



District to mineral-scale geometry of the world-class Antino orogenic gold system, southeastern Suriname (Guiana shield)

Vincent Combes^{a,*}, Aurélien Eglinger^{b,c}, Pascal Voegeli^a, Rayiez Bhoelan^d, Carlos Bertoni^e, Colin Padget^a, Anne-Sylvie André-Mayer^b

^a Founders Metals Inc., Vancouver, Canada

^b GeoRessources, Université de Lorraine, Nancy, France

^c Norda Stelo, Québec, Canada

^d Witlage and Associates, N.V. Paramaribo, Suriname

^e Advisor, Brazil

ARTICLE INFO

Keywords:

Orogenic gold
Intrusion-hosted
Shear zone
Multiscale
Vein analysis
Guiana shield

ABSTRACT

The Antino-Yaou-Benzdorp gold district (Eastern Suriname), located within the Rhyacian-aged Marowijne Greenstone Belt of the Guiana Shield, hosts multiple gold deposits preferentially developed within intermediate intrusive bodies (intrusion-hosted orogenic gold) and at lithological boundaries (shear zone-hosted orogenic gold). A multi-scale approach, integrating district- to ore-mineral-scale observations is applied to assess the geometry and structural controls on gold mineralization. Within the district, the spatial distribution and orientation of gold camps, such as the Antino gold camp, are controlled by the TTG-complexes locations and shapes. These rigid bodies act as buttress for strain accumulation within the volcano-sedimentary sequence. At the deposit scale, zones of enhanced deformation are located at lithological contacts, along antiformal limbs, and along the edges of tonalitic intrusive bodies. These intrusions were preferential hosts for later brittle deformation and related brecciation/veining. The first compressional stage D₁, produced the ENE fabric, while the second stage, D_{2a}, was responsible for the main folding event during ongoing compression under NE-SW-oriented shortening, and the formation of axial planar fabric S_{2a}. NW-oriented dip-slip shear zones are related to the D_{2b} deformation stage and host both metric fault-fill veins and progressively deformed tension vein arrays. Locally, a refolding of the S_{2b} mylonitic foliation is observed (D₃ deformation-stage). This progressive ductile deformation is then locally overprinted by a polyphase brittle deformation (D₄) stage expressed by breccias, extensional veins and fractures. Strain axis orientations for shearing (NE-SW shortening) and refolding of mylonitic segments (NW-SE shortening) control the location of low-stress sites and, therefore, the location and orientation of gold ore shoots. At the mineral scale, micro X-ray fluorescence scanning on core samples reveals that early D_{2b} veins act as ground preparation sites for later (D₃ and D₄-related) gold deposition, with boudin necks and folded mylonite hinges serving as low-stress zones for pyrrhotite and gold deposition. The D₄-related brittle overprinting plays an important role in the total gold budget with remobilization and/or new gold inputs. Both shear zone-hosted, and tonalite intrusion-hosted systems demonstrate the importance of rheology in building an orogenic gold system. This study emphasizes the value of integrating multi-scale data for gold targeting, particularly through detailed vein analysis, which should be applied across the entire Guiana Shield.

1. Introduction

When documenting and predicting the geometric architecture of an orogenic gold system (Groves et al., 1998; Goldfarb et al., 2001, and references therein), a scale-sensitive approach is essential to assess the different structural controls on gold mineralization (e.g., Robert and

Brown, 1986; Robert et al., 1994; Allibone et al., 2002; Allibone et al., 2018; Feybesse et al., 2006; Wyman et al., 2016; Lebrun et al., 2016; Masurel et al., 2017; Masurel et al., 2021; Chauvet, 2019; Blenkinsop et al., 2020; Perret et al., 2020; Combes et al., 2021a, 2022, 2024; Sumail et al., 2024; among others).

Paleoproterozoic gold districts are proximal to craton-scale

* Corresponding author.

E-mail address: vincentc@fdrmetals.com (V. Combes).

<https://doi.org/10.1016/j.oregeorev.2025.106575>

Received 20 December 2024; Received in revised form 17 March 2025; Accepted 18 March 2025

Available online 18 March 2025

0169-1368/© 2025 The Authors. Published by Elsevier B.V. This is an open access article under the CC BY license (<http://creativecommons.org/licenses/by/4.0/>).

structures that serve as first-order ore-forming fluid pathways (Groves et al., 2000; Goldfarb et al., 2005; Robert et al., 2004) whilst individual, camp- to deposit-scale controlling features, are usually related to second or third-order structures (Cassidy et al. 1998; Blenkinsop et al., 2000; Feybesse et al., 2006; Dubé and Gosselin, 2007; Groves et al., 2018).

Such camp- to deposit-scale structural features, acting as fluid conduits, preferentially develop at lithological contacts, at margins of intrusive bodies, in high-angle reverse fault zones or within antiformal fold structures with increased deformation/fluid flow at hinges, fold neck and/or limbs (e.g. Robert and Brown, 1986; Sibson et al., 1988; Hodgson, 1989; Cox et al., 1995; Goldfarb et al., 2005; Vearncombe and Zelic, 2015; Groves et al., 2018; Gaboury, 2019; Blenkinsop et al., 2020; Cox, 2020). In these contexts, rheology is a key factor in controlling the spatial distribution of gold deposition that led to the formation of (1) preferential sites for strain accumulation (e.g. lithological contacts, intersections of structures, bending of structures) and (2) sites of enhanced dilation (i.e. fluid focusing) caused by changes in attitude, splays, intersections segmentation, stepovers or releasing bends along shear/fault structures (Peters, 1993; Micklethwaite et al., 2010; Blenkinsop et al., 2020 and references therein). Identifying low mean stress sites at all scales is critical as they represent preferential hydrothermal fluid pathways and favorable sites of focused fluid flow.

Finally, the influence of folding of the mylonitic fabric (and related *syn*-shearing tension vein arrays) with local bending/deflection of shear

segments, producing a dilation site for vein development and enhanced sulfide deposition, is also a key parameter for gold upgrading (Peters, 1993; Feybesse et al., 2006; Lacroix et al., 2024; Berthier et al., 2024; among others). The importance of competence contrast is also observed when localized late-stage brittle deformation is preferentially overprinting preexisting gold-bearing ductile shear zones (i.e., ground preparation with for example a shear zone that was previously silicified: Peters, 1993) and shear-related preexisting veins producing low-stress sites that will focus the deposition of subsequent veining and sulfides (Siddorn, 2010) with possible gold enrichment (i.e., gold mobility related to deformation: Tomkins and Mavrogenes, 2002; Cook et al., 2013; Voisey et al., 2024) in a polyphase/progressive deformation context (Thébaud et al., 2018; Perret et al. 2020; McDivitt et al. 2022; Combes et al. 2021a; Sumail et al., 2024; Berthier et al., 2024).

The intrusion-hosted subclass of orogenic gold deposits is a typical example of rheological control where more competent units, such as intrusive bodies affected by regional deformation, are preferential hosts for gold-bearing extensional vein development compared to the volcano-sedimentary hosting lithologies (e.g., Allibone et al., 2004; Tourigny et al., 2018; Combes et al., 2021a; Masurel et al., 2021). Importantly, the structural architecture of gold mineralization should be assessed from the larger considered scale (most commonly the district scale) to the mineral scale using various characterization techniques such as structural interpretations using geophysics, field mapping, oriented drill

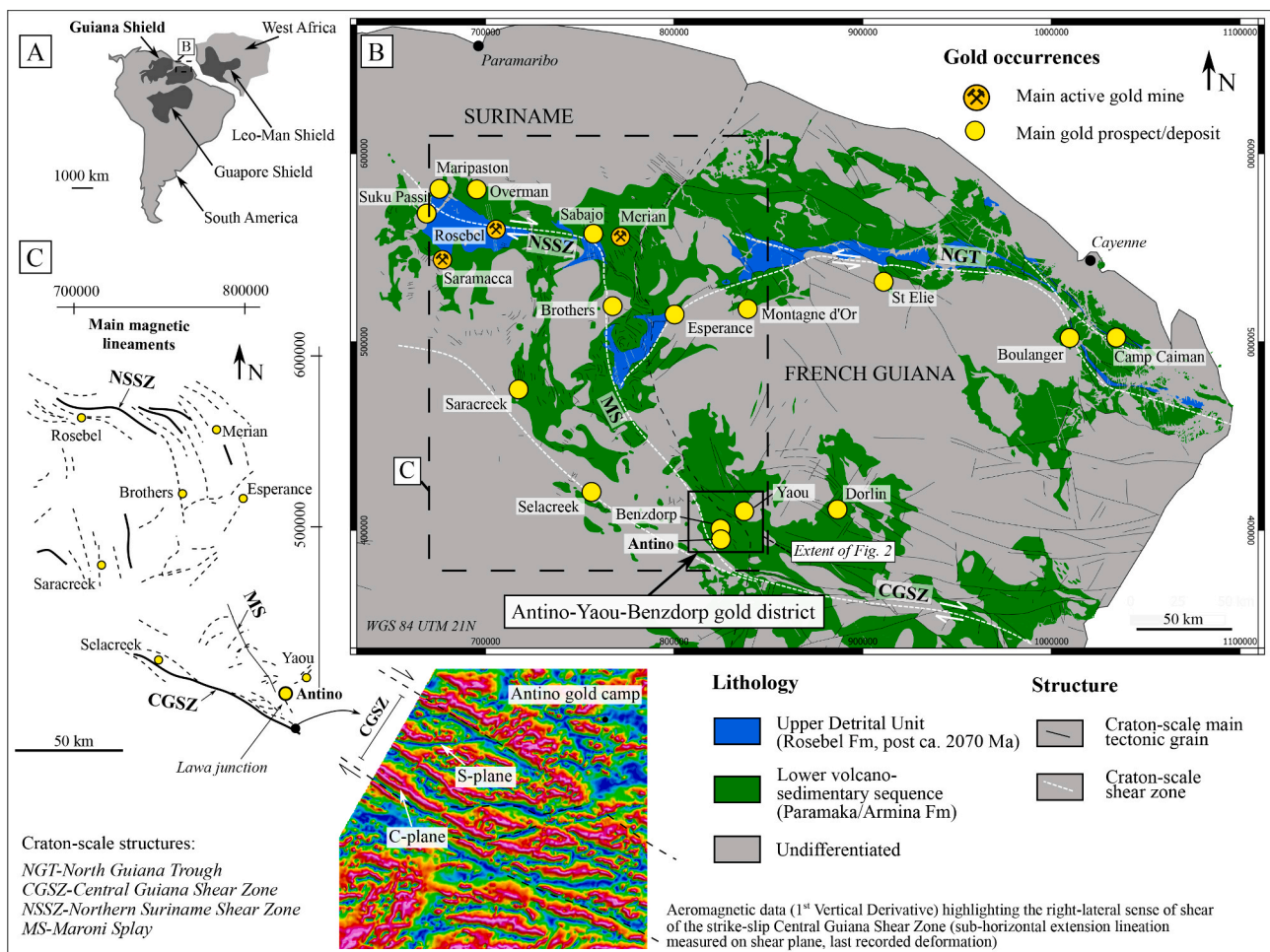


Fig. 1. A. Location of the Guiana Shield in South America with its counterpart in Western Africa. B. Structural framework and main gold occurrences in the NE part of the Guiana Shield modified from Kroonenberg et al. (2016) and Delor et al. (2003a) highlighting the spatial distribution of the Rhyacian Marowijne greenstone belt and Upper Detrital Unit over Suriname and French Guiana with the location of the Antino-Yaou-Benzdorp gold district. Major craton-scale shear zones are named after Ledru et al. (1991) and Voicu et al. (2001). C. Main magnetic lineaments and spatial relation with the main gold occurrences of Suriname and western French Guiana (see extent in B) based on the Suriname and French Guiana airborne magnetic data.

cores analysis and detailed microstructural studies. In this scheme, predictions of prospective sites can be made and then field-tested (Cowan, 2020).

The Antino gold system, located in the prolific Antino-Yaou-Benzdorp gold district (AYB district, (Fig. 1A-B-C)) in southeastern Suriname (NE Guiana Shield, Kioe-A-Sen et al., 2016; Kroonenberg et al., 2016; Combes et al., 2022), is here chosen as a case study to document the geometry and spatial distribution of a complex mineralized gold system. This paper describes the structural patterns, hydrothermal alteration, vein system and sulfide deposition, with respect to deformation, from the district to the mineral grain scale.

We combine multiscale litho-structural data with detailed macro- and microstructural analysis using μ XRF scanning of entire drill cores to evaluate the geometry and structural controls on the gold mineralization. The results have strong implications for improving mineral exploration strategies within the Antino concession, the AYB gold district, and the Guiana Shield as a whole.

2. Geological settings

2.1. Northeastern Guiana Shield

The Transamazonian Province, located in the northeastern portion of the Guiana Shield (Fig. 1A and B), comprises metavolcano-sedimentary sequences and associated tonalite-trondhjemite-granodiorite (TTG) rocks of Rhyacian age (Vanderhaeghe et al., 1998; Delor et al., 2003a; Delor et al., 2003b, and references therein). Two Archean nuclei, the Imataca Complex in Venezuela to the northwest and the Amapá Block in Brazil to the southeast (Gibbs and Barron, 1993), are recognized within this province. Younger terranes within the Guiana Shield have been identified, younging from the SW to the NE part of the craton (Gibbs & Barron, 1993; Delor et al., 2003a; Kroonenberg et al., 2016).

The Rhyacian rocks were accreted and deformed over four key deformation/geodynamic stages during the Transamazonian Orogeny (ca. 2260 Ma to 1950 Ma; Ledru et al., 1991; Vanderhaeghe et al., 1998; Delor et al., 2003a; Delor et al., 2003b). The initial deformation stage (D_1) stage is related to a subduction phase with crustal growth and back-arc terrane formation (ca. 2180–2130 Ma). D_1 was followed by the D_{2a} stage, marking the end of subduction in a collisional context, characterized by tectonic accretion and crustal reworking during a compression to transpression phase (ca. 2110–2080 Ma, Pb-Pb on zircon, Delor et al., 2003a). The D_{2b} stage (ca. 2070–2060 Ma, on the basis of syn-tectonic quartz-monzonite intrusions in French Guiana U-Pb dating on zircon, Delor et al., 2003a, Delor et al., 2003b) is marked by dextral strike-slip shearing and crustal stretching (Vanderhaeghe et al., 1998; Delor et al., 2003b). The late D_{2c} stage, associated with granulite facies metamorphism, is dated to ca. 2000–1993 Ma (De Roever et al., 2003; Delor et al., 2003a, Delor et al., 2003b; Klaver et al., 2015).

The diversity of gold mineralization types, observed in the Guiana shield, highlights the various geodynamic environments in which they formed and deformed (Goldfarb et al., 2001; Bierlein et al., 2002; Eglinger et al., 2020) and their polyphase formation with multiple gold-forming events (Milesi et al., 2003; Bardoux, 2019, 2022; Combes et al., 2021a). An overview of the major gold deposits of the Guiana Shield is given in Table 1. Examples include the volcanogenic massive sulfide (VMS) deposit at Montagne d'Or in French Guiana, where sulfide mineralization is interpreted as coeval with arc magmatism (Franklin et al., 2000; Guiraud et al., 2020); the orogenic intrusion-hosted Yaou deposit in French Guiana (Milesi et al., 2003; Combes et al., 2021a, Combes et al., 2022) and the Omai deposit in Guyana (Bertoni et al., 1991; Voicu et al., 2001); the sediment-hosted Rosebel and Merian orogenic gold deposits in Suriname (Watson et al., 2008; Daoust et al., 2011; Bardoux et al., 2017); the intrusion-related Las Cristinas deposit in Venezuela (Ristorcelli and Spencer, 2007) and the overprinting of pre-tectonic strata-bound sulfide deposit by a later orogenic gold system at Dorlin, French Guiana (Milesi et al., 2003 and Bertoni et al., 2019).

The proposed comparison table (Table 1) highlights the importance of a proximal intrusion that acts mostly as a favorable host for vein development (rheological control, intrusion-hosted orogenic gold deposits, IHOG) or as a more rigid body for strain accumulation at margins within the volcano-sedimentary package.

2.2. Eastern Suriname

Eastern Suriname (Fig. 1B, C) is underlain by the lower volcano-sedimentary sequence commonly referred to as the Paramaka Formation for the volcanic to volcano-sedimentary units and the Armina Formation for the sedimentary rocks with low grade metamorphism (Gibbs and Barron, 1993; Ledru et al., 1991; Delor et al., 2003a, Delor et al., 2003b; Kroonenberg et al., 2016, and references therein). These units are unconformably overlain by shallow marine sedimentary rocks, known as the Rosebel Formation in Suriname (Daoust et al., 2011 after Watson et al., 2008) or the Upper Detrital Unit in French Guiana (Milesi et al., 1995; Delor et al., 2003b). Plutonic rocks associated with the regional D_1 stage display a TTG-like geochemical and mineralogical signature. In French Guiana, two generations of TTG rocks have been identified: one dated to ca. 2183–2155 Ma and another to ca. 2152–2144 Ma and ca. 2140–2120 Ma (Delor et al., 2003b; Enjoly, 2008; Combes et al., 2022). In Suriname, these tonalite, trondhjemite, and granodiorite batholiths, often ellipsoidal in shape, are considered as a single unit, referred to as the Kabel Tonalite (Bleys, 1951), without subdivision.

Within these formations, regional shear zones have been identified, such as the Central Guiana Shear Zone (CGSZ), which strikes WNW–ESE and forms a splay referred to as the Maroni Splay (Voicu et al., 2001, Fig. 1B, C) that strikes NNW. To the north, this structure merges with the North Suriname Shear Zone (NSSZ, Fig. 1B, C). The Antino-Yaou-Benzdorp gold district lays at the intersection of the CGSZ and the Maroni Splay, now referred to as the Lawa junction (Fig. 1C).

3. Materials and methods

Observations were made and structural measurements collected at (1) the district scale (aggregate of mineralized camps with dimensions ranging from 10 to 100 km; here the Antino-Yaou-Benzdorp gold district, Fig. 2A), (2) the camp scale (cluster of deposits with dimensions varying from 1 to 10 km; here the Antino concession with gold deposits such as Upper / Lower Antino, Buese or Lawa, Fig. 2A), (3) the deposit scale (a set of mineralized bodies relatively closed to each other, less than a km; here the Upper Antino deposit with its mineralized structures such as Froyo or Donut, Fig. 3), (4) the macroscopic scale (oriented diamond drill core, mm – 100 m, Figs. 9–13), and (5) the mineral grain scale (from a few centimeters to the micron (Figs. 14–17)). The definitions of Jébrak and Marcoux (2008) are followed regarding the terms *district*, *camp*, and *deposit* scale.

In this context, the investigation of structural controls on gold mineralization is based on the following methods:

(i) Structural interpretations using both aeromagnetic data and digital elevation models. For the entire district and the Antino gold camp, structural interpretations are drawn from aeromagnetic surveys (Founders Metals Inc. for Antino-Benzdorp and Combes et al., 2022 for Yaou) and a digital elevation model (LiDAR data set from Founders Metals Inc.). Airborne magnetic surveys are particularly useful for identifying structures and lithologies, allowing the building of litho-structural maps (Jessell et al., 1993; Betts et al., 2007; Aitken and Betts, 2009; Baratoux et al., 2015; Combes et al., 2022), especially in undercover domains (with deep weathering profiles, Metelka et al., 2011). Filters used include the First Vertical Derivative (1VD) and the Tilt Derivative (TD). A shaded digital elevation model from the northwest is also used. At the deposit scale, structural lineaments were mapped using new chargeability and resistivity anomaly maps derived from an electrical ground survey (electrical resistivity tomography and

Table 1
Comparison of major Au deposits of the Guiana Shield (all references are mentioned in the table).

Gold system	Antino (within the AYB district)	Yaou (within the AYB district)	Merian	Brothers	Rosebel	Oko West	Omai	Aurora	Karouni	Dorlin	Montagne d'or	Boulanger	Las Cristinas
Country	Suriname	French Guiana	Suriname	Suriname	Suriname	Guyana	Guyana	Guyana	Guyana	French Guiana	French Guiana	French Guiana	Venezuela
Available research study	<i>This study</i>	Combes et al., 2021a; Combes et al., 2022	Bardoux, 2017	Combes et al., 2024	Watson et al., 2008; Daoust et al., 2011	Hainque et al., 2024	Bertoni et al., 1991; Voicu et al., 2001	G2 technical report	Tedeschi et al., 2018a; Tedeschi et al., 2018b	Milesi et al., 2003; Bertoni, 2019	Franklin et al., 2000; Guiraud et al., 2020	Lacroix et al., 2024	Ristorcelli et al., 2007
Au endowment (Moz)		~1,5	~6		~13	~6	~6	~6	~1	~1,6	~4		~17
Deposit type	Orogenic gold	Orogenic gold	Orogenic gold	Orogenic gold	Orogenic gold	Orogenic gold	Orogenic gold	Orogenic gold	Orogenic gold	Pre-tectonic stratabound sulfide and Orogenic gold overprinting	Volcanogenic massive sulfide (VMS)	Orogenic gold	Porphyry system and Orogenic gold overprinting?
Intrusion-hosted orogenic gold?	Partly IHOG, metric tonalitic intrusive bodies	Mostly IHOG, metric Qz monzodiorite intrusive bodies	No	IHOG, kilometric tonalitic batholith (TTG)	No	No	Mostly IHOG, metric Qz monzodiorite intrusive bodies	Partly IHOG, dioritic intrusive bodies	No	No	No	No	No
Proximal intrusion?	Donut tonalite, Froyo diorite, Buese tonalite (...)	Yaou Qz monzodiorite	None	Kabel tonalite	Brincks tonalite	Purini batholith and Oko pluton (granodiorite/diorite)	Omai stock (Qz monzodiorite) and felsic dykes	Rory's Knoll diorite	Karouni Qz monzonite, Hicks granodiorite	Metric granitoid dykes	<i>Dark and Pale</i> QFP	None	Diorite dyke, Monzonite sill
Deformation and structural controls on gold mineralization	Polyphased, NW dip-slip shear zones, local refolding and brittle overprinting	Polyphased, NE shear zone and brittle deformation hosted by NE trending intrusive bodies	Polyphased, NW antiform, NW reverse shear zones, fold hinges	Polyphased, ENE ductile shear zones locally overprinted by late brittle deformation	WNW strike-slip shear zone, and E-W shear zone	Polyphased, folding, reverse shearing, then compressional phase with brecciation	WNW shear zone, multi-stage brittle deformation and veining	NW dip-slip shear zone	NW dextral strike-slip shear zones	Polyphased, NW to N-S shear zone, early stage Tur-sulfide mineralization	Stratiform sulfide dissemination, layers of deformed semi-massive sulfide	Polyphased, WNW shear zones, followed by transcurrent deformation event with refolding	NNE trend, breccia pipe and disseminated stratabound mineralization

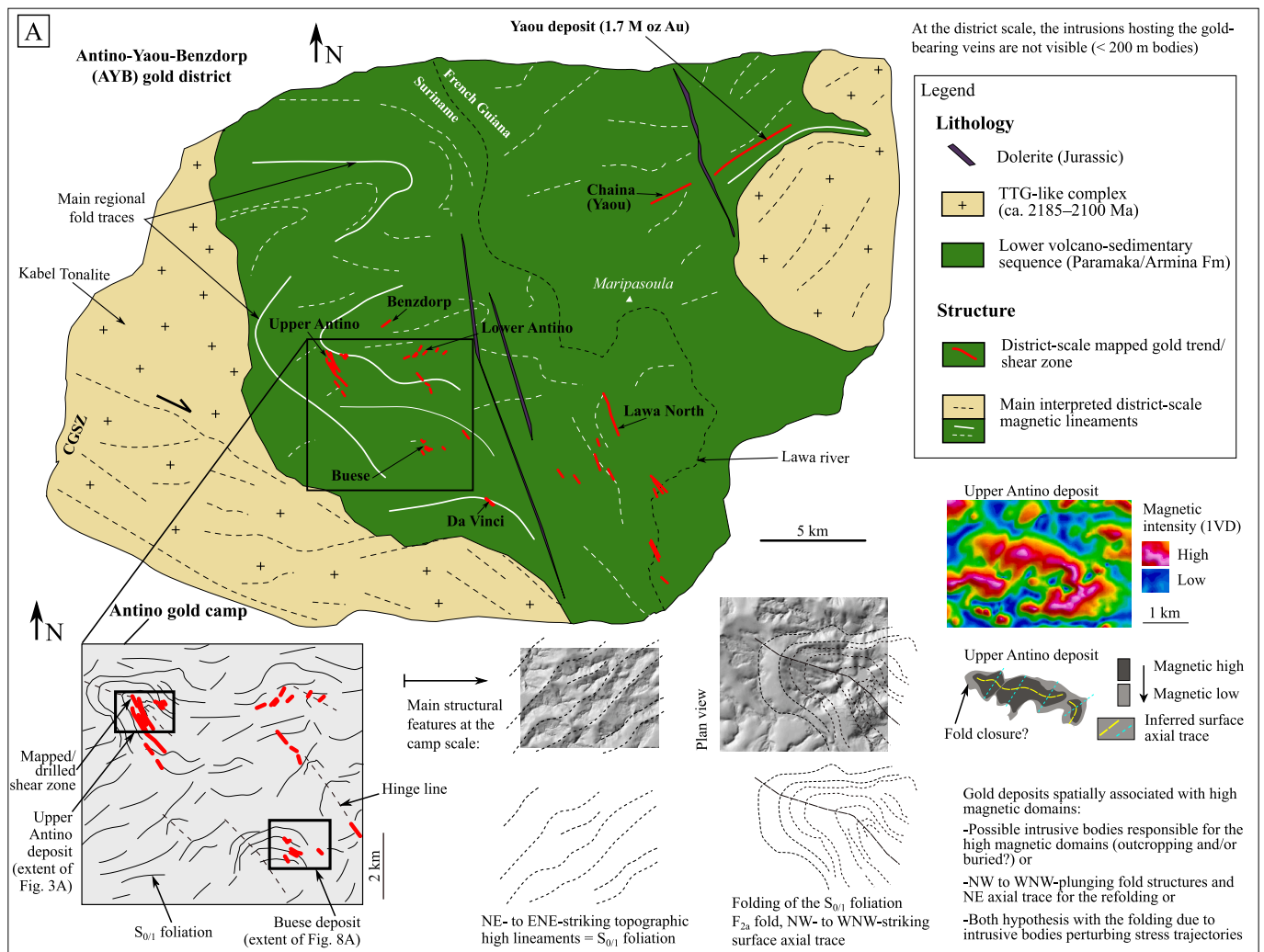


Fig. 2. A. New district-scale and camp-scale geological maps using available airborne magnetic and topographic data sets of Founders Metals Inc. and Combes et al. (2022). Main mapped gold trend/shear zones are indicated for the whole district. Main ENE-striking tectonic grain and localized folding with NW-striking hinge lines are indicated at the camp scale. The aeromagnetic signature of the Upper Antino deposit is presented and interpreted as resulting from the NW-plunging antiform and/or a buried magnetic-high intrusion. Geographic coordinates are omitted for confidentiality issues. B. Summary of the deformation stages, vein system, main hydrothermal alteration, and gold mineralization features observed at the camp to mineral scale. A progressive ductile deformation sequence is locally overprinted by a polyphase brittle deformation. (Abbreviations, ev: extensional vein, ffv: fault-fill vein, tva: tension-vein array).

induced polarization with pole-dipole and gradient arrays at 37.5 m inter-electrode spacings) surveyed by GexplOre.

(ii) Structural mapping involving detailed examination of surface outcrops, particularly those exposed by small-scale mining activities. The region is covered mainly by a well-developed regolith and equatorial rainforest, representing a challenging environment for exploration and mapping (Freyssinet et al., 1989, 2005; Butt, 1998, 2015; Thévenaut and Freyssinet, 2002; Anand and Butt, 2010; Combes et al., 2021b). Structural measurements are recorded in strike/dip (right-hand rule) and linear data as plunge/azimuth. These data are plotted on equal-area stereograms using the lower hemisphere convention (STEREONET software, Allmendinger et al., 2012). All deformation stages mentioned in this study are specific to the Antino deformation sequence except when dealing with regional deformation scheme of Delor et al. (2003a, 2003b and references therein).

(iii) Detailed drill core logging of over 60 oriented and 45 unoriented diamond drill holes (drilled by Founders Metals Inc.). Intervals of 100 cm–150 cm are described depending on the core, to accurately document variations in the different lithologies and alteration assemblages related to the vein types. The veins are described based on their

generation, their cumulated corrected thickness, the sulfides generation, the type of sulfide and sulfide grain count. Particular attention is given to quantifying the strain intensity, with an empirical coding of strain intensity considering both the grain size reduction (compared to undeformed rock, confirmed at the microscopic scale) and the shear fabric intensity (foliation development). The collected data are plotted against Fire Assay gold values to provide comprehensive documentation of gold distribution in relation to different structural parameters (Figs. 9–10). Alpha, beta and gamma angle measurements are collected using a goniometer to assess the fabric and vein orientations, kinematics, and geometry following the methods described in Blenkinsop et al. (2015) and Holcombe, (2016). These measurements are used to produce a detailed petro-structural framework with deformation stage sequences and vein classification, following the definitions of Sibson (1990), Robert et al. (1994) and Laing (2004) (i.e., sigmoidal to planar tension vein arrays, tva; laminated fault-fill vein with host rock slivers, ffv; or post-shearing brittle single planar extensional vein, ev) in which gold events can be evaluated in term of contribution to the total gold endowment. Drill hole sections were produced using the Leapfrog Geo software 2023.2 with drill hole data management by Rogue Geoscience.

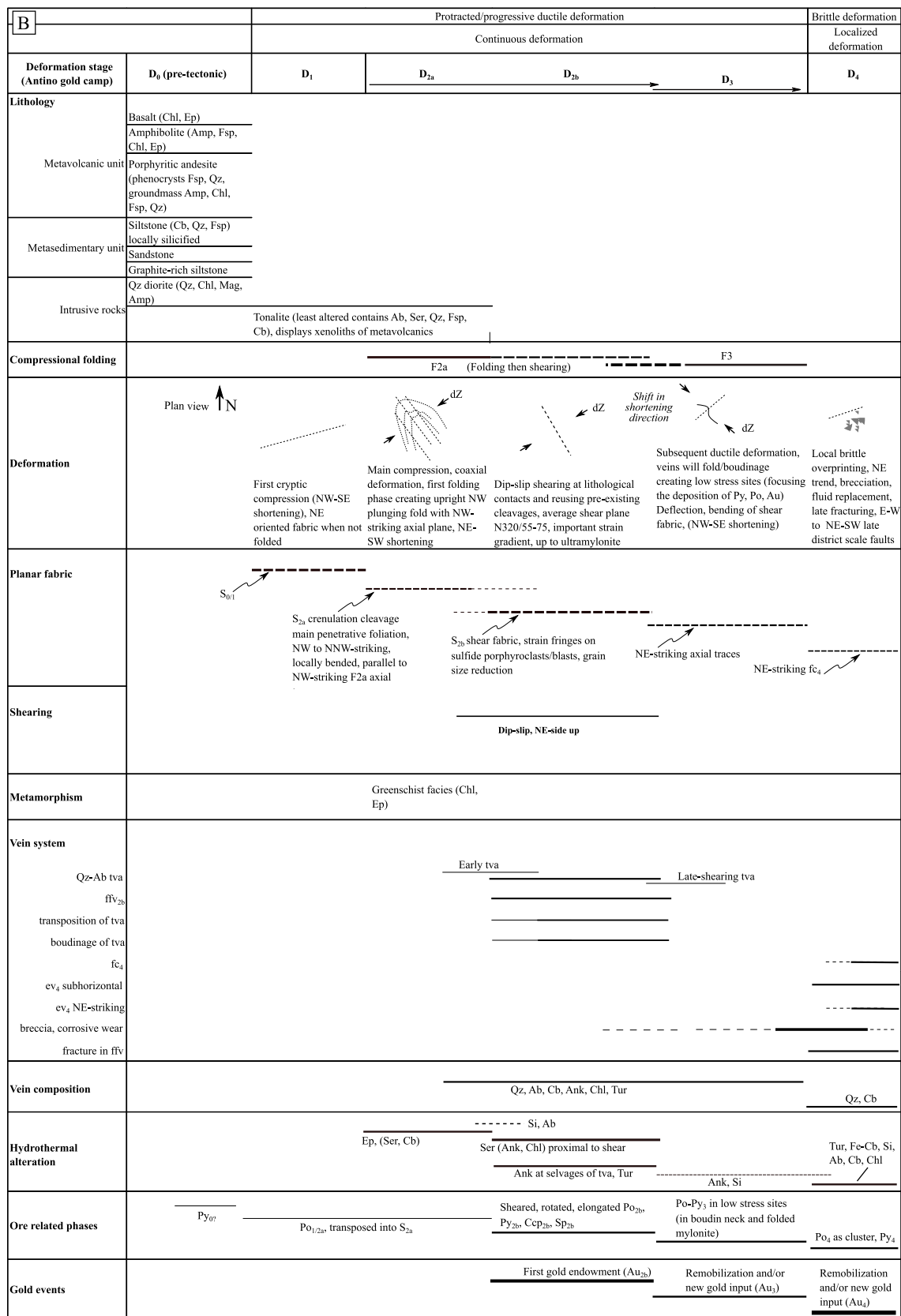


Fig. 2. (continued).

And (iv) microscopic analytical work based on 20 polished thin sections. Microfabric characterization, mineral identification, overprinting relationships, and ore parageneses were studied with optical,

reflected and transmitted light microscopy at the GeoResources laboratory (Nancy, France). Sulfide minerals were examined using a TESCAN scanning electron microscopy (SEM) to characterize ore assemblages

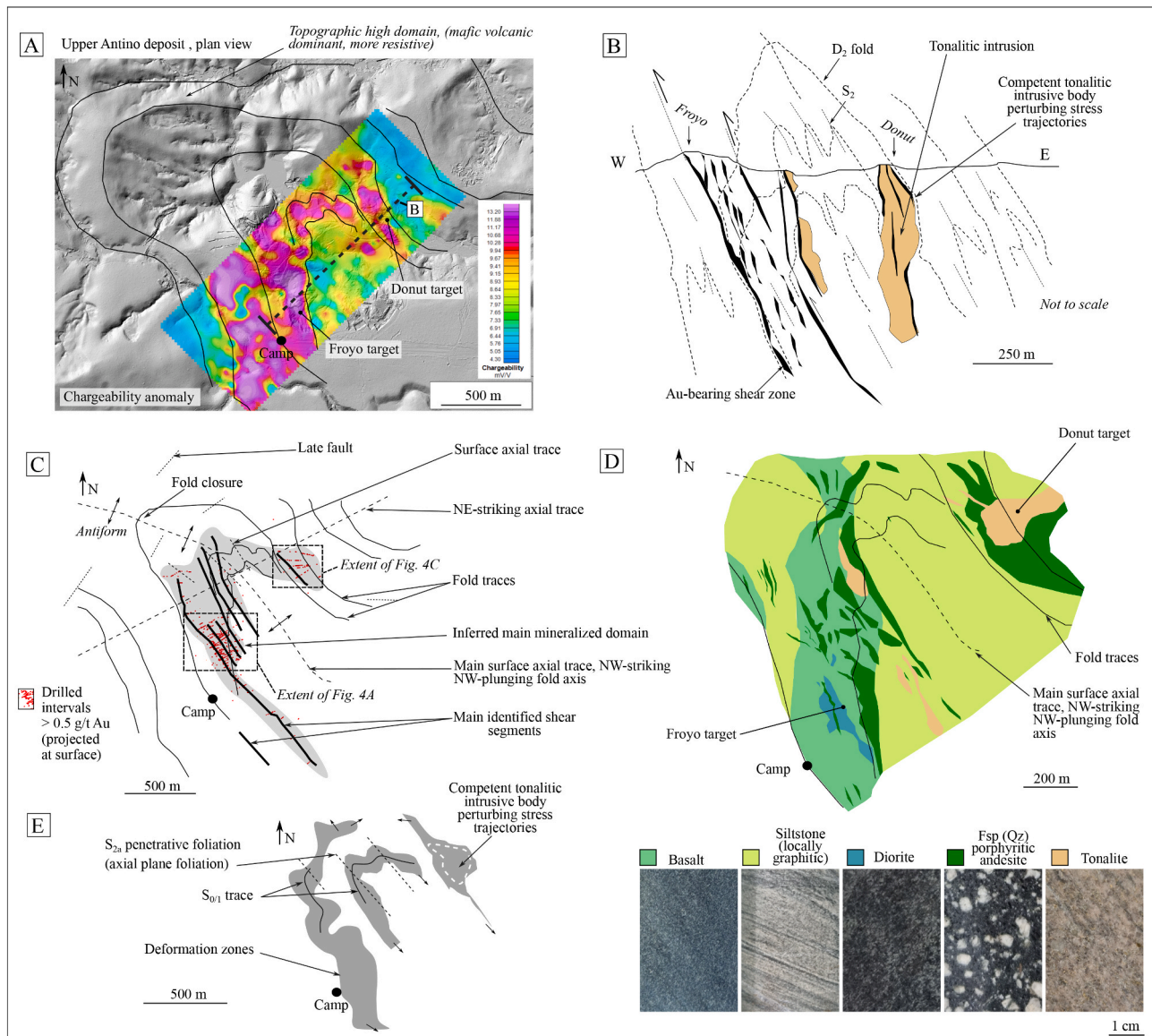


Fig. 3. A. Chargeability map derived from ground Induced Polarization survey and shaded high-resolution digital elevation model, acquired by LiDAR, showing the main interpreted fold traces and drill targets for the Upper Antino deposit. B. Synthetic litho-structural section of Upper Antino (see A for location) indicating the Froyo gold-bearing shear zone and the main occurrences of the tonalite bodies. C. Simplified structural pattern of the central part of the Upper Antino deposit. D. Spatial distribution of main lithological units based on mapping and diamond drill holes projected at the surface. E. Identified domain with increased deformation within the Upper Antino deposit.

and pyrite morphology. The SEM analyses were conducted using the backscattered electron mode (BSE) with typical beam conditions of 15 kV and 10nA with an SEM equipped with an Energy-dispersive X-ray spectrometer (EDS) at the GeoRessources laboratory (Nancy, France). Micro-XRF geochemical maps were produced using a Bruker Tornado μ XRF scanner at GeoRessources laboratory (Nancy, France) with a 30- μ m step size, 15 ms/pixel, and 50-kV acceleration voltage. Eleven half-drill core samples were selected. Bruker's AMICS software package was used for mineral identification from μ XRF spectra using an XRF spectra library matching and detailed evaluations of XRF spectral attributes. Both element and mineral distribution maps (single and mineral mixture per pixel) are produced for each drill core sample.

4. Results

4.1. District-scale structural patterns

At the southern border between French Guiana and Suriname, the Antino-Yaou-Benzdorp gold district records a complex deformation history as illustrated by the new proposed litho-structural map (Fig. 2A). The combined available airborne magnetic datasets allow us to identify, to the southwest of the gold district, the first order craton-scale shear zone (right lateral motion) first referred to as the Central Guiana Shear Zone (CGSZ) by Voicu et al. (2001) with a WNW-ESE direction. The two main TTG-like complexes are located at the NE and to the SW of the district. The one to the SW is identified as the Kabel Tonalite by Bley (1951) and Kroonenberg et al. (2016), while the batholith situated to the NW (in French Guiana) is referred to as a TTG-like complex of a second generation (i.e. dated at ca. 2140–2120 Ma; Delor et al., 2003b). In between these intrusive complexes, a deformed volcano-sedimentary

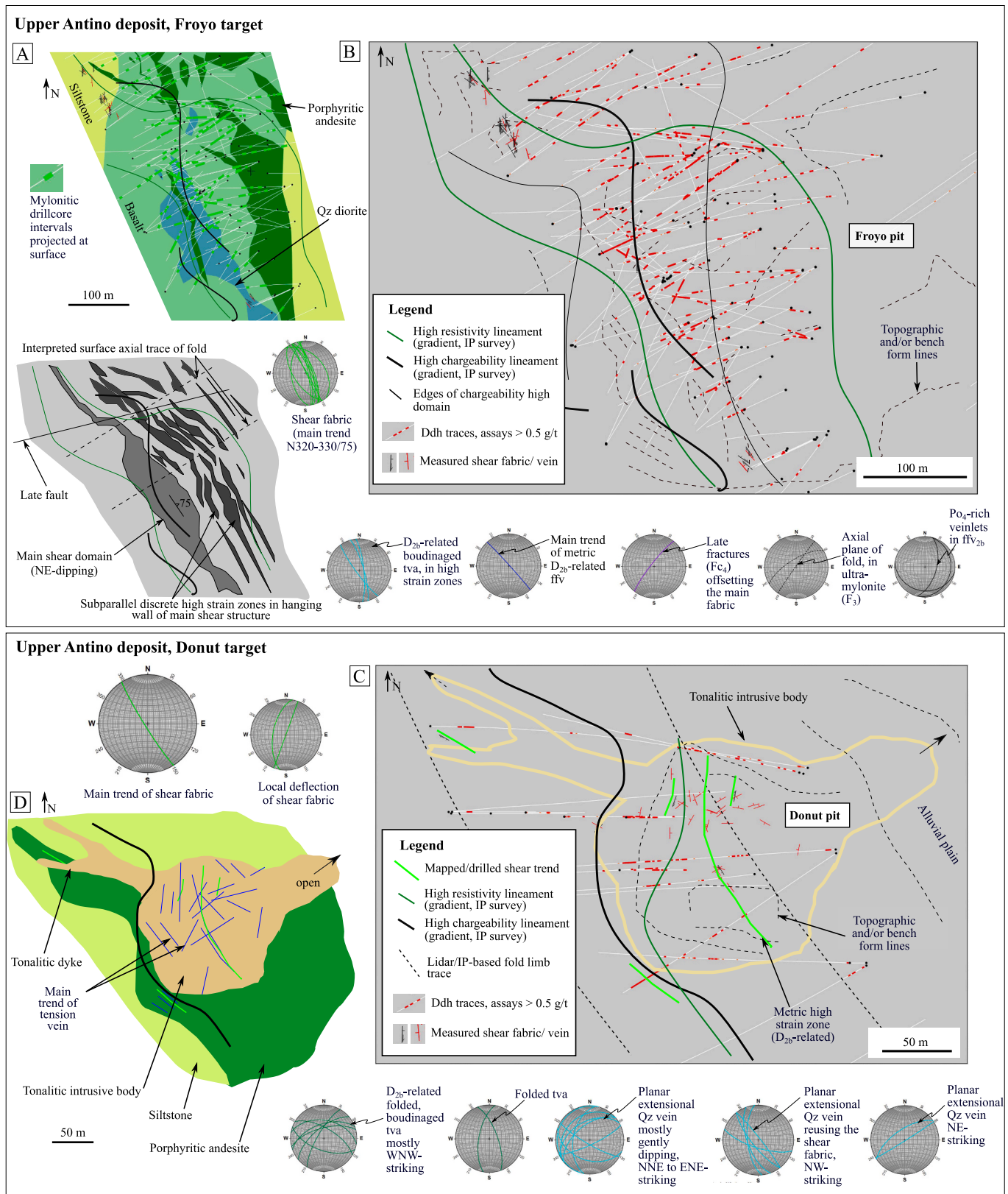


Fig. 4. Litho-structural framework of the Froyo and Donut gold-bearing structures with A. Distribution of mylonitic drill core intervals at Froyo, projected at surface, and host lithologies with outlines of mineralized zones developed along the shear segments. B. Overview of mineralized drill core intervals and resistivity-chargeability lineaments at Froyo. Note that gold zones are preferentially developed when these lineaments are curved. C. Outlines of the tonalite intrusion at Donut with mapped high-strain zones, veins and mineralized drill core intervals. D. Schematic plan view of the Donut structure, with veins preferentially hosted by the tonalite body.

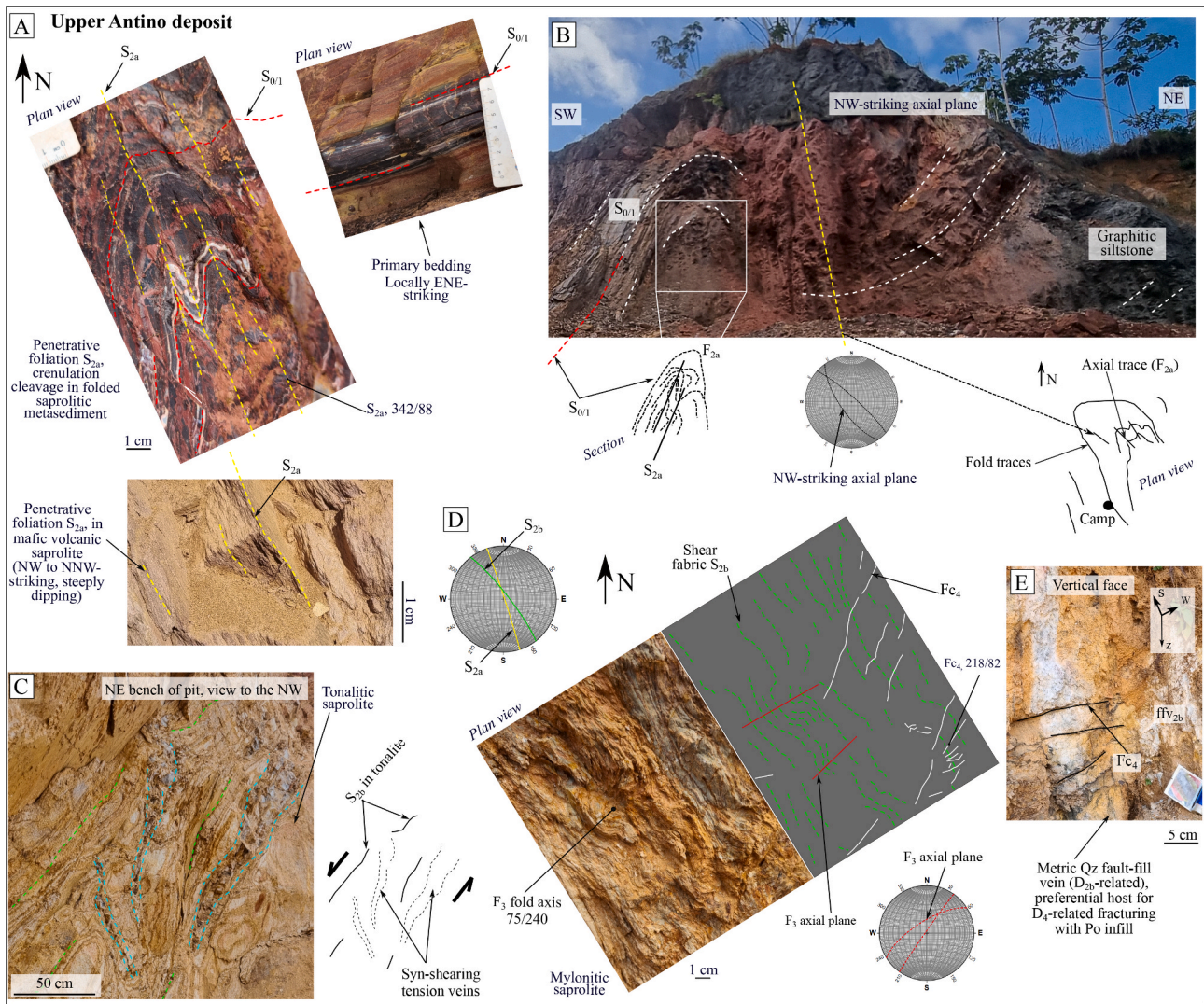


Fig. 5. Structural elements from the Upper Antino deposit with photograph of A. Metasediments with $S_{0/1}$ traces and crenulation cleavage S_{2a} (penetrative foliation). B. Plunging upright fold in sediments with an NW-striking axial plane. C. High-strain zone in tonalite with *syn*-shearing tva_{2b} . D. Mylonitic foliation S_{2b} with local microfolding (NE axial traces). E. Sub-horizontal fractures F_{c4} preferentially developed in preexisting massive fault-fill vein (ffv_{2b}).

sequence is observed where newly identified lineaments show a complex folded pattern with NE- to E- to ESE-striking axial surfaces (Fig. 2A). A dominant ENE-striking tectonic/magnetic grain is observed as well, while NW-striking features are identified to the SE of the district. Late dolerite dikes crosscut the district with an NNW orientation. The gold trends (shear zone and/or intrusion-hosted mineralized domains mapped by the authors) indicated in Fig. 2 are located, from W to E, at Upper Antino (NW-trending structure), Benzdorp (NE-trending structure), Buese (WNW-trending structure), Lower Antino (NE-trending structure), Lawa north and south (NNW-trending structure) and at Yaou-Chaina (NE-trending structure). At this scale, the strikes of the main shear zones are subparallel to the orientation of the nearest lithological contacts between the TTG-like batholiths and the (wrapped around) volcano-sedimentary sequences (see discussion).

4.2. Camp-scale structural patterns

When downscaling to the camp scale, the orientation of the main tectonic grain visible on LiDAR imagery is ENE to NE-oriented and is expressed mainly by topographic highs and lows lineaments (Fig. 2A, ridges and alluvial plains). This dominant fabric is locally folded (Fig. 2A) creating NW-striking hinge lines and distinct fold closures (e.

g., the Upper Antino structure, see next section). The second area of interest for this study, referred to as the Buese deposit, displays an NW-striking alluvial plain) that offset and crosscut the main ENE topographic lineaments. As an example, the main magnetic domains for Upper Antino (using 1VD and Tilt Derivative grids) are delimited in Fig. 2. Surface axial traces are oriented WNW and then refolded with a second axial trace, creating interference patterns (and plunges toward the W to NW, similar to the fold closures identified with the LiDAR but not exactly at the same location), suggesting two main folding phases (Type 2 interference pattern of Ramsay (1962)). An alternative interpretation (see discussion section) would identify the magnetic high domains as magnetic intrusive bodies (locally buried), with strain accumulation located around the bodies. The drawn axial trace would then correspond to the central part of intrusions. The intersection zones of the two axial traces correspond to gold enrichment zones. This association has been verified in eight different locations while mapping and/or observing small-scale miner activities. At the scale of the Antino camp, the mapped shear zones are also preferentially located where the ENE dominant fabric is folded with an NE-SW shortening (Fig. 2A).

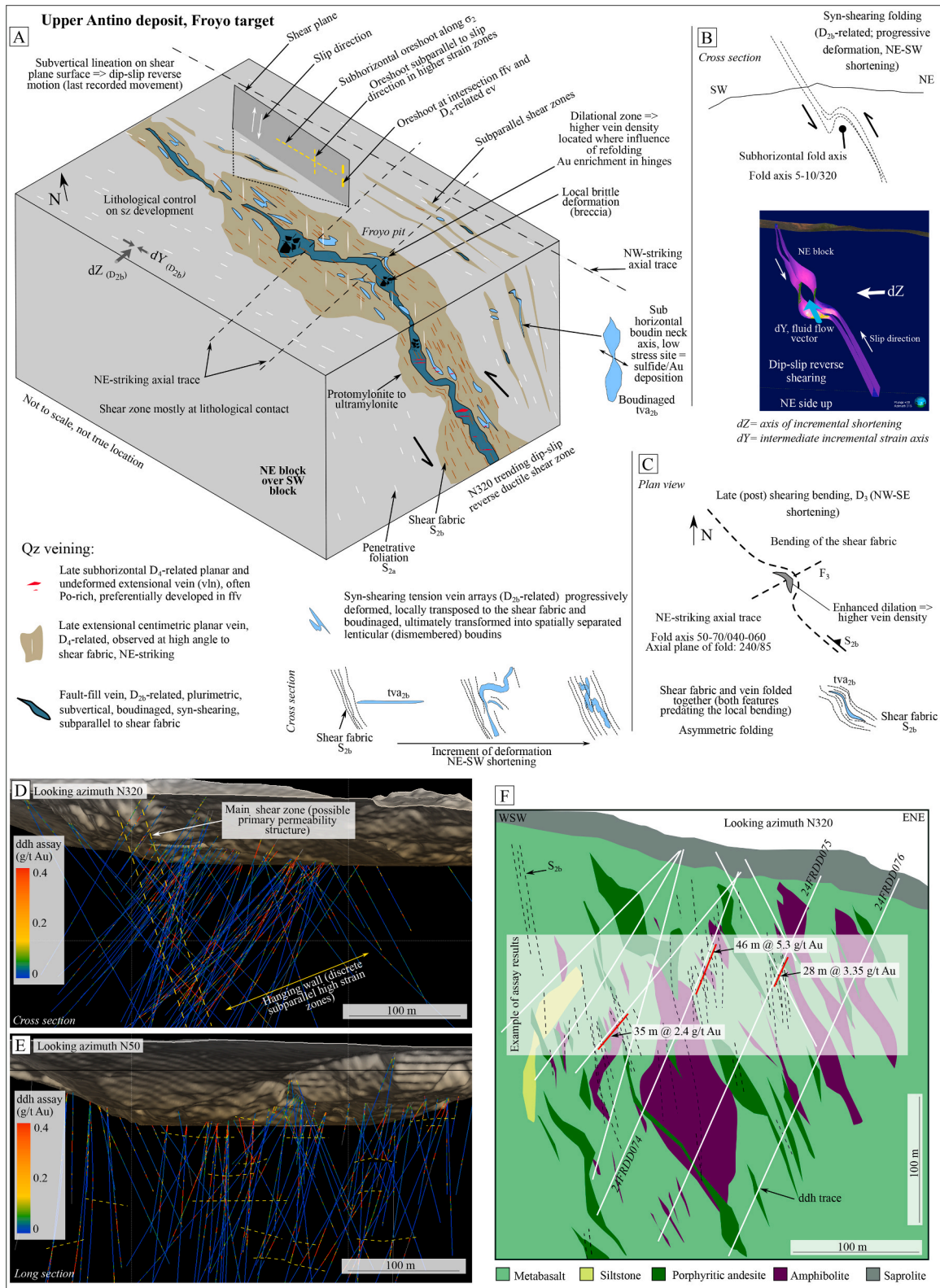


Fig. 6. A. Sketch illustrating the structural setting of the Froyo structure with emphasis on the different vein types associated with the shear zone. B. Sketch illustrating the syn-shearing folding (D_{2b}-related; progressive deformation, NE-SW shortening) of the mylonitic foliation and of the entire Froyo structure with development of sub-horizontal fold axis. C. Plan view illustrating the late-shearing bending/deflection of both the shear fabric and the syn-shearing tension veins (both features predating the local bending), enhanced dilation in newly formed hinges resulting in higher vein density. D. Gold distribution and drill holes traces in cross section (view orthogonal to the shear trend, i.e., N320) showing the main shear zone (NE dipping) and the multiple discrete subparallel metric shear segments to the E. E. Gold distribution and drill holes traces in long section view (NW-SE) highlighting the multiple sub-horizontal ore shoot trends. F. Cross section through the Froyo structure (looking azimuth N320), illustrating the multiple steep northeast dip of sheared (D_{2b}-related), altered (Ser-Ank) and mineralized zones.

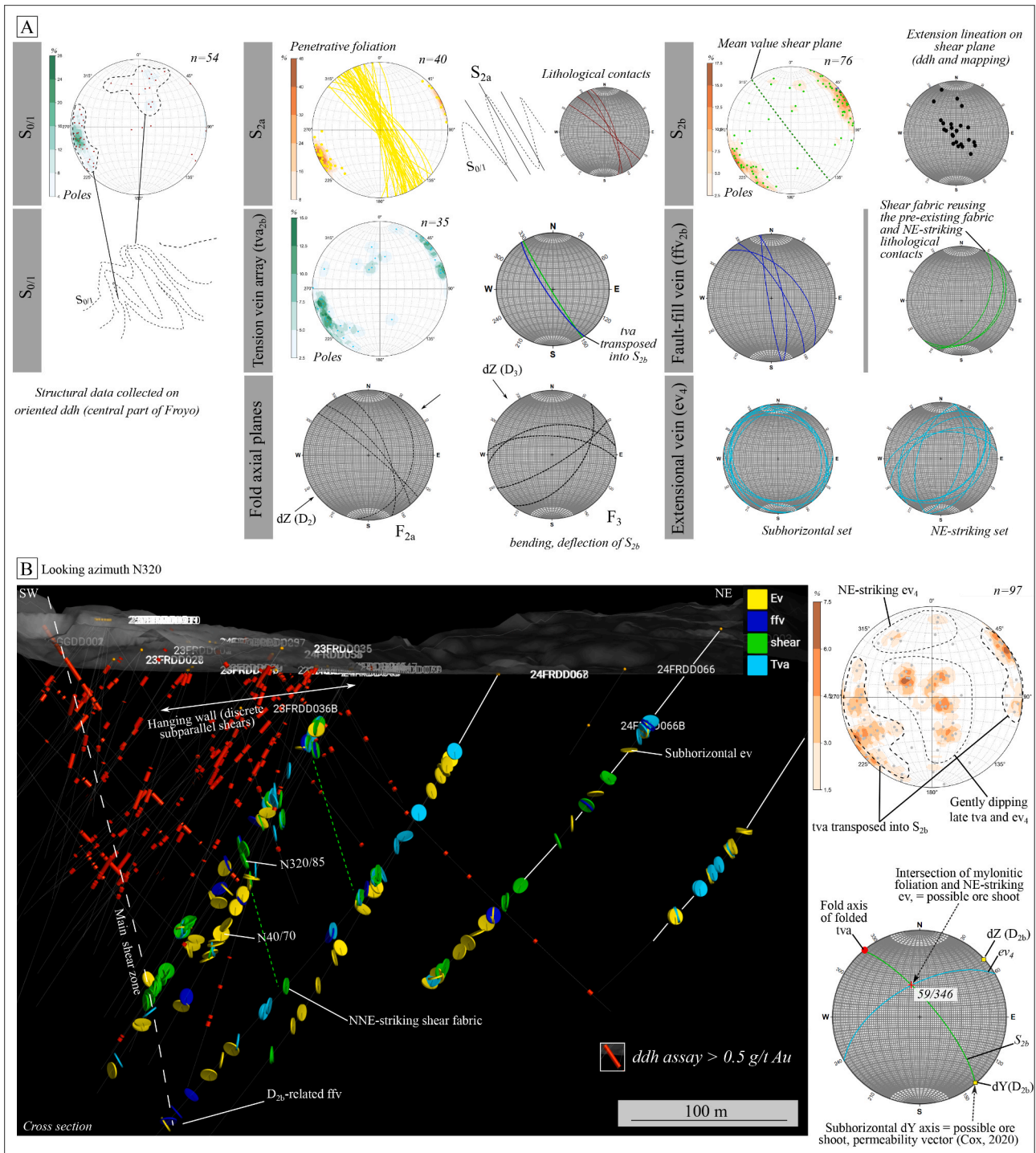


Fig. 7. A. Stereogram of key structural features measured on oriented diamond drill cores at Froyo (Schmidt projection, equal area and lower hemisphere). B. Cross-section view (looking azimuth N320) of the Froyo structure with diamond drill hole assays and planar structural data displayed as disks (extracted from Leapfrog Geo) for ffv, tva, ev and shear fabric (Abbreviations, ev: extensional vein, ffv: fault-fill vein, tva: tension-vein array).

4.3. Deposit-scale geometry of the Upper Antino and Buese deposits

Within the Antino gold camp, the Upper Antino deposit and the Buese deposit are considered for this study (Fig. 2A). The structural scheme outlined for the Upper Antino and Buese deposits is summarized in Fig. 2B.

4.3.1. The Upper Antino deposit

The host rocks are dominated by a volcano-sedimentary sequence

metamorphosed to greenschist facies with (1) a Chl-rich basalt, (2) a sedimentary unit composed of siltstone, sandstone and graphitic-rich siltstone, (3) a Fsp- (Qz)- porphyritic andesite, (4) a micro Qz diorite and (5) a tonalite. Their simplified spatial distribution (based on drill hole projected at the surface and a few saprolite exposures) is shown in Fig. 3. These units have undergone moderate to high-strain deformation, localized mostly along the limbs (locally at the hinges) of an antiform structure (Fig. 3A) and at the edges of the tonalitic bodies (for example, at the Donut drill target) where these competent bodies are perturbing

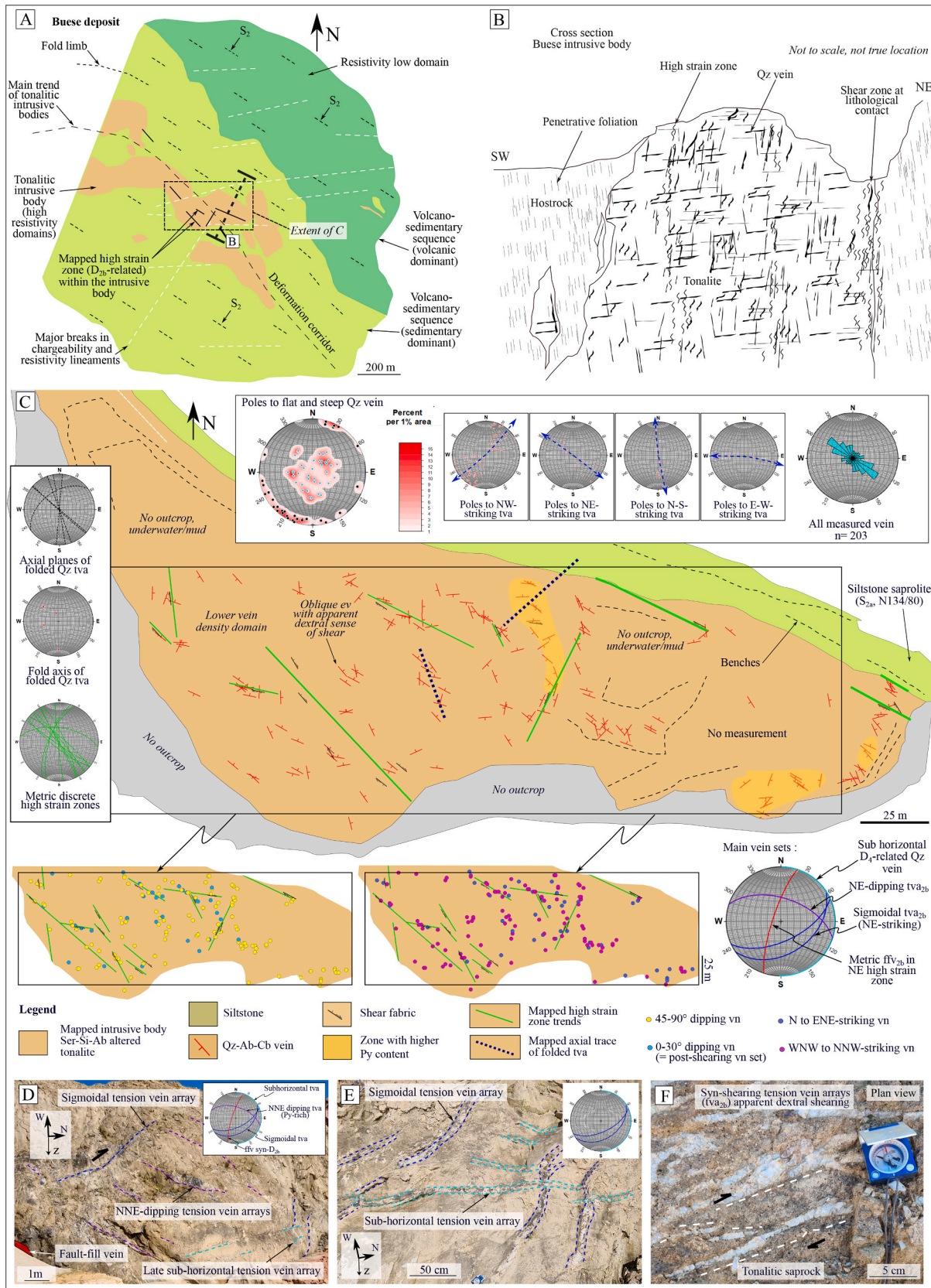


Fig. 8. A. Geological map of the Buése deposit showing the WNW-oriented intrusive body trend, B. Synthetic litho-structural section across the tonalite body in the central part of the Buése deposit (see A for location). Coordinates are omitted for confidentiality issues. C. Schematic map of the Buése tonalitic body with collected structural data at the surface (small open pit). The tonalite has sponsored fracture development (veining) due to its competent nature, the internal high-strain zones (in green) being the main fluid pathways within the rigid tonalitic bodies. D-E. Syn-shearing sigmoidal and planar tension vein arrays developed in a tonalite body. F. Stack of NNE dipping tva_{2b} hosted by the tonalite.

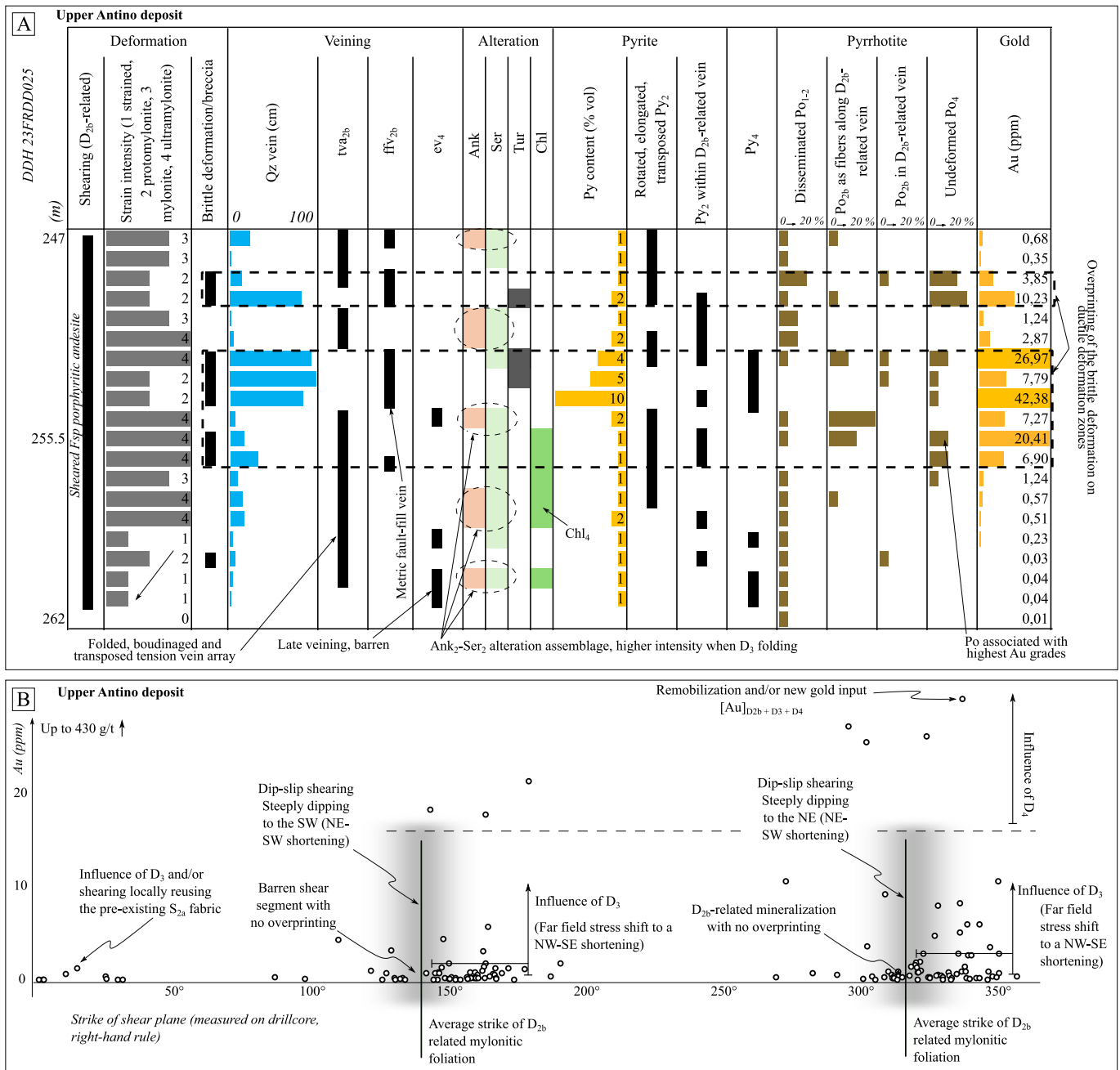


Fig. 9. A. Example of vertical correlations between the different structural-lithological data of drill core 23FRDD025 (central part of Froyo). Observed/measured parameters collected every 1 m along the investigated scanlines are plotted against the gold content per interval to identify what controls the grades. Note the association between the gold grade content and both the vein density (and associated pyritization) and the overprinting of brittle deformation on preexisting ductile deformation. (Abbreviations, Ank: ankerite, Ser: sericite, Tur: tourmaline, Chl: chlorite, Py: pyrite, Po: pyrrhotite, Qz: quartz, ev: extensional vein, ffv: fault-fill vein, tva: tension-vein array). B. Gold grade (ppm) versus the strike of shear fabric (measured on drill cores) at the Froyo drill target illustrating the influence of both the refolding of the shear fabric (D₃) and the brittle overprinting (D₄) on gold endowment.

the stress trajectories. Importantly, the main trends of the gold-bearing shear zones often follow/exploit the preexisting fabrics (D₁-related).

The Upper Antino deposit is characterized by a 2 km wide antiform with a NW-plunging fold axis and a NW to WNW-trending axial plane, identified by both topographic and chargeability anomaly maps (Fig. 3A, B). This asymmetrical, slightly overturned and isoclinal fold displays a fold closure to the NW of the study area (the zone of closure has not yet been explored). The topographic high domain can be followed along the two limbs of the fold, while the main hinge zone corresponds to a topographic low domain. The chargeability anomalies form a symmetrical sequence with high and low domains following the

fold's limbs (low chargeability on outside limbs and higher chargeability on central limbs with a moderate to low response in the inner part in the SE). Within this fold structure, the location of the different drill targets is indicated in Fig. 3A. The chargeability domains and edges of high-low responses also evidence some tight M-type parasitic folds (Fig. 3A), as illustrated in the cross-section in Fig. 3B. The Froyo drill target (Fleming, 2006) corresponds to a gold-bearing shear structure (D_{2b}-related, Fig. 2B) on the W limb of the fold (D_{2a}-related, Fig. 2B), while the Donut drill target is mainly a tonalitic body with multiple shear zones (D_{2b}-related, Fig. 2B) in the NE limb (Fig. 3A, B). In this framework, the main mapped/drilled shear segments are subvertical, NW-

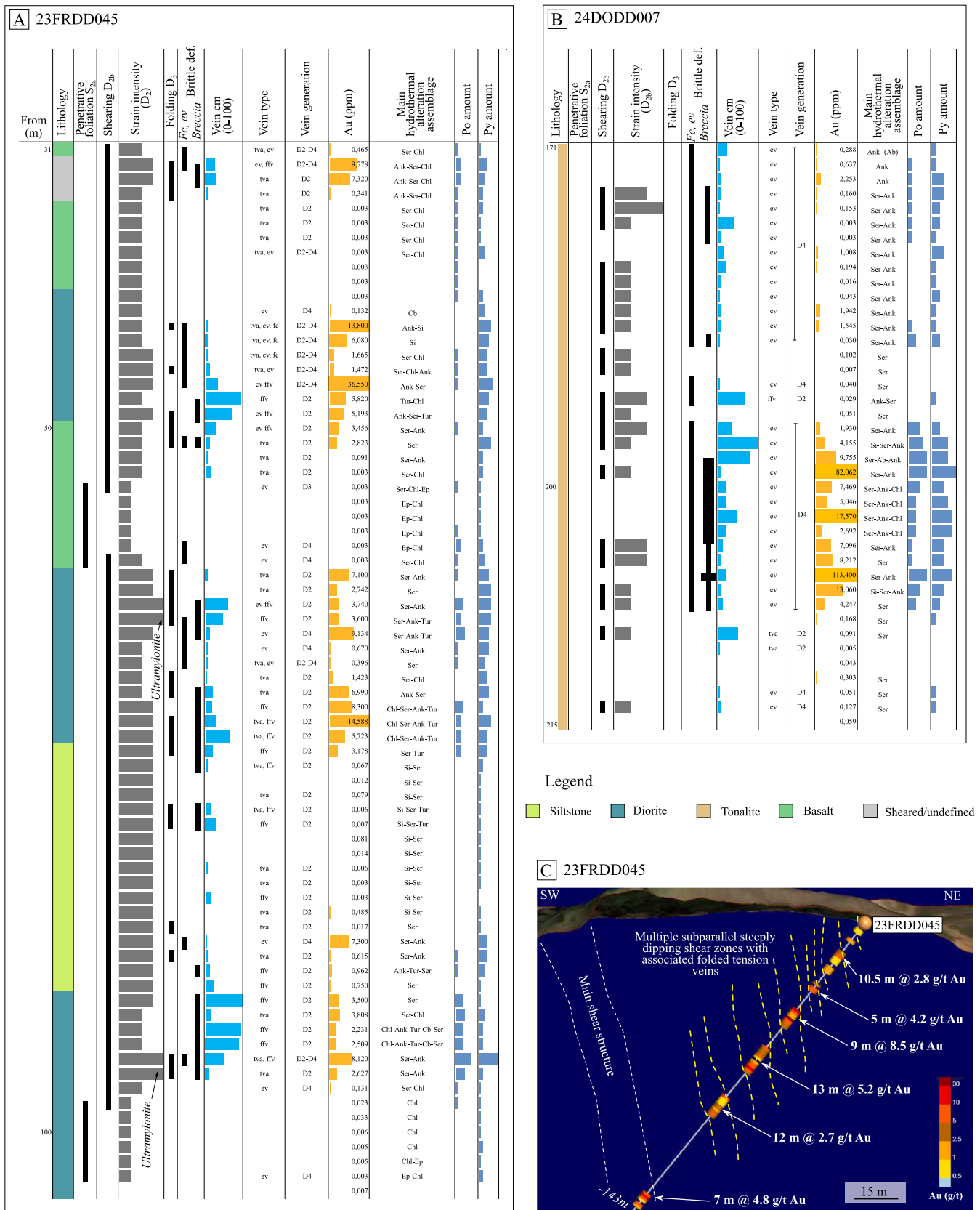


Fig. 10. Example of vertical correlations between the different structural-lithological data in drill cores for the Froyo structure (A, and corresponding cross-section with drill hole trace and grades in C) and for the Donut structure (B). Observed/measured parameters collected every 1 m along the investigated scanlines are plotted against the gold content per interval to identify what controls the grades. The gold content distribution is related to the strain intensity (D_{2b} -related), the degree of folding of the mylonitic foliation, the vein density and associated alteration (mostly Ank), and sulfide content (syn- and post-shearing deposition). The amount of observed brittle deformation/brecciation correlates with the highest gold grades. (Mineral abbreviations as in Fig. 9A).

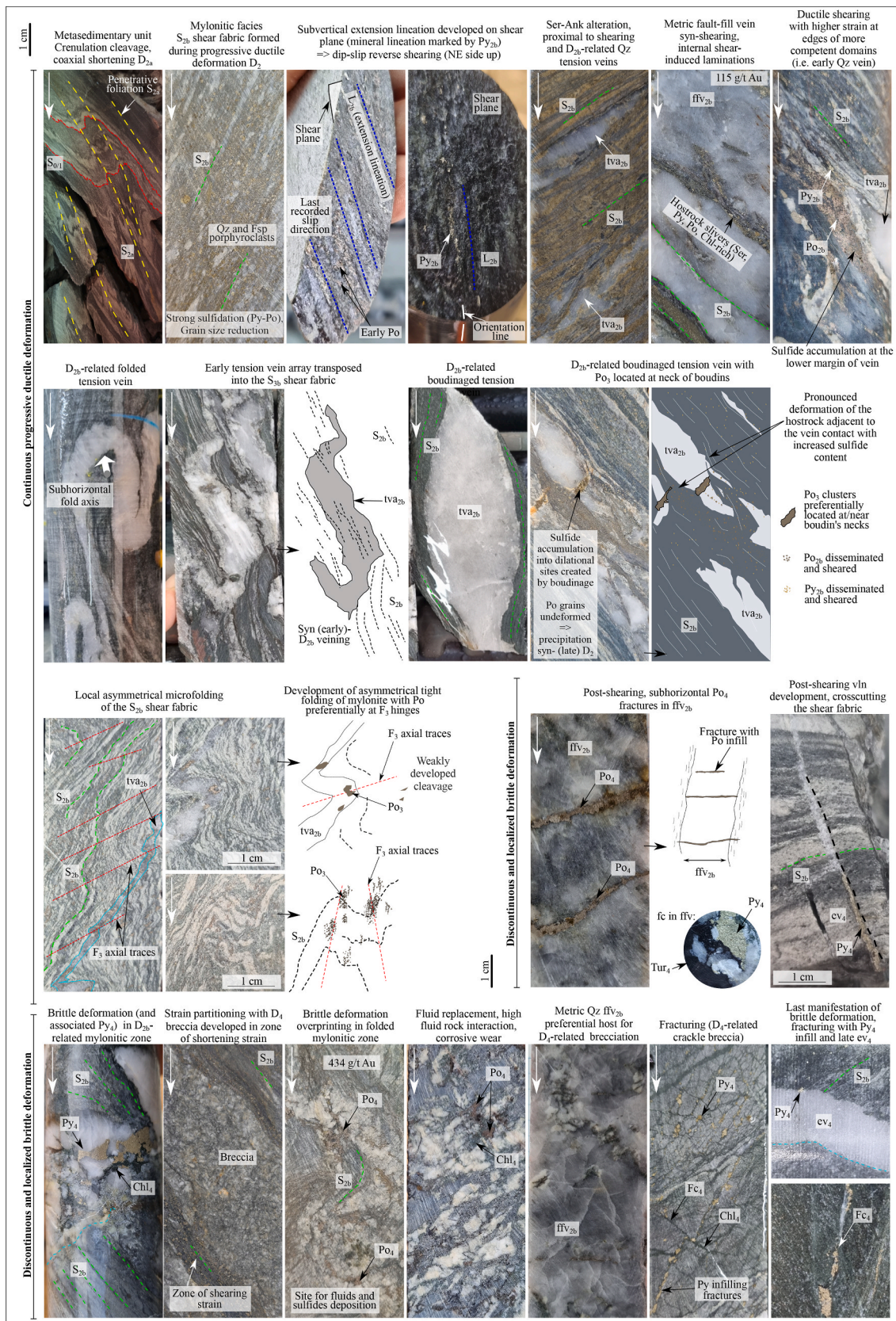


Fig. 11. Summary of key macroscopic expressions of the progressive ductile deformation and localized brittle deformation on drill cores at Froyo. See text and Fig. 2B for relative chronological constraint explanation. Mineral abbreviations as in Fig. 9A, (fc: fracture).

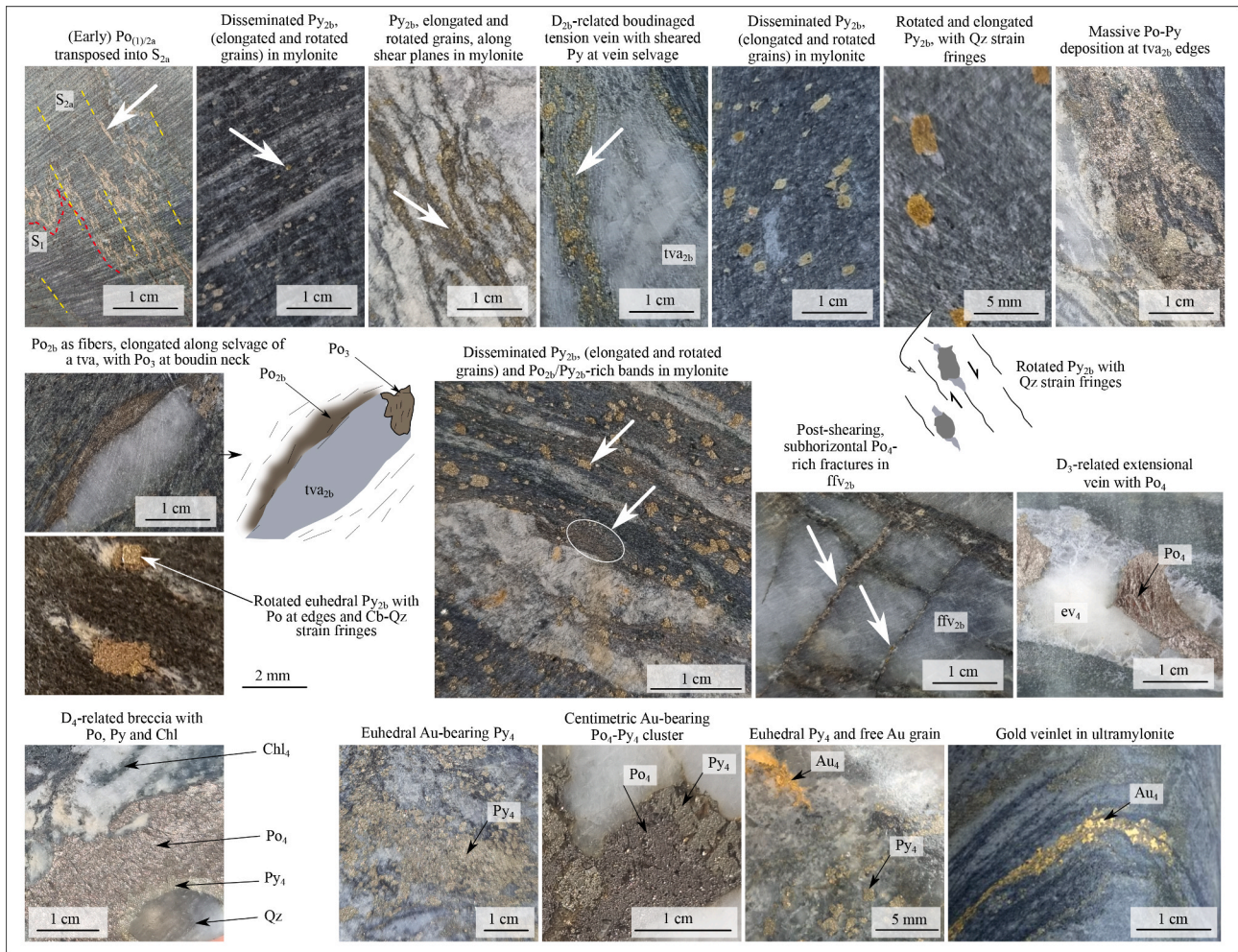


Fig. 12. Summary of the ore-related phases identified at the macroscopic scale on drill cores at Froyo.

trending, and subparallel to the main identified fold limbs (Fig. 3A, B, C). These gold-bearing structures (D_{2b} -related, Fig. 2B) locally crosscut the limbs and the pre-shearing fabrics (D_1 and D_{2a} -related, Fig. 2B). The penetrative foliation (axial plane traces of the NW folds, S_{2a}) has a NW to NNW trajectory, while an earlier fabric ($S_{0/1}$, see mapping/drill core scale sections) is mostly ENE-striking, and locally NW-striking when transposed by the penetrative foliation S_{2a} . Locally chargeability high-low lineaments experienced some bending with NE-striking axial traces. The topography-based fold traces of the entire structure are also refolded (D_3 stage, Fig. 2B) with an NE-striking axial plane. Late NE-striking faults offset the topographic lineaments (Fig. 3A and C) and possibly linked to the D_4 deformation stage.

4.3.2. Geometry of the Froyo target

At the Froyo drill target Fig. 4A, B), the gold mineralization is associated with a zone of intense non-coaxial shearing (steeply dipping, NE-side-up, dip-slip shear zone trending N320/75 and related to the D_{2b} deformation stage). This structure, mapped and drilled in the Froyo pit, has returned high-grade intervals such as 38 m @ 10.90 g/t Au and 45.79 m @ 4.06 g/t, for example. Outside the kilometre structure, a penetrative foliation related to the D_{2a} compressive deformation stage with NE-SW shortening is observed (Fig. 5A), with local cryptic D_1 deformation and $S_{0/1}$ foliation, S_{2a} being the crenulation cleavage with NW axial plane (Fig. 5B). These two foliations are rarely preserved within the shear zone. The deformation corridor, dipping to the NE and up to 300 m wide, is composed of a main decametric ductile shear zone to the W with multiple subparallel metric shear zones in the hanging

wall to the E (Fig. 4A, B). The strain is preferentially accommodated by lithological contact zones, especially at contacts between the porphyritic andesite and the other lithologies such as the basalt, the siltstone and the microdiorite. The shear zone is marked by protomylonitic to ultramylonitic facies with well-developed anastomosing shear fabric (Fig. 5D), referred to as S_{2b} (related to the D_{2b} deformation stage, Fig. 2B). The shearing is poorly developed inside the basalt or the siltstone, while wider shear intervals are observed within the porphyritic andesite. Local bending and deflection of the shear segments are observed in outcrops (NE-striking axial planes, Fig. 5D) and correlate with the pattern of chargeability-resistivity based lineaments (Fig. 4A, B). This deformation, with NW-SE shortening, is related to the last increment of the progressive ductile deformation D_2 and is referred to as the D_3 deformation stage (Fig. 2B). Brittle deformation (polyphase D_4 deformation stage, Fig. 2B) is locally recorded as sub-horizontal fractures in preexisting D_{2b} -related metric fault-fill veins, as localized crackle breccia, and as NE-striking fractures at a high angle to the mylonite (Fig. 5D). An overview of the geometry of the structure is given in Fig. 7A, with an emphasis on the vein types and different folding features observed at the deposit scale. The whole deformation corridor hosts a complex vein system (Fig. 6A) with (1) *syn*-shearing metric Qz-Cb fault-fill veins (ffv_{2b}) displaying shear-induced laminations (wall-rock clasts that were progressively dissolved) and sinuous styloliths, (2) centimetric (early)-*syn* shearing folded and boudinage Qz-Ab-Cb-Ank tension veins arrays (tva_{2b}) and (3) planar, post-shearing, D_4 -related, single Qz-Cb extensional veins (ev_4) that are crosscutting the shear fabric and the D_2 -related veins. These veins are shallow dipping and NE-

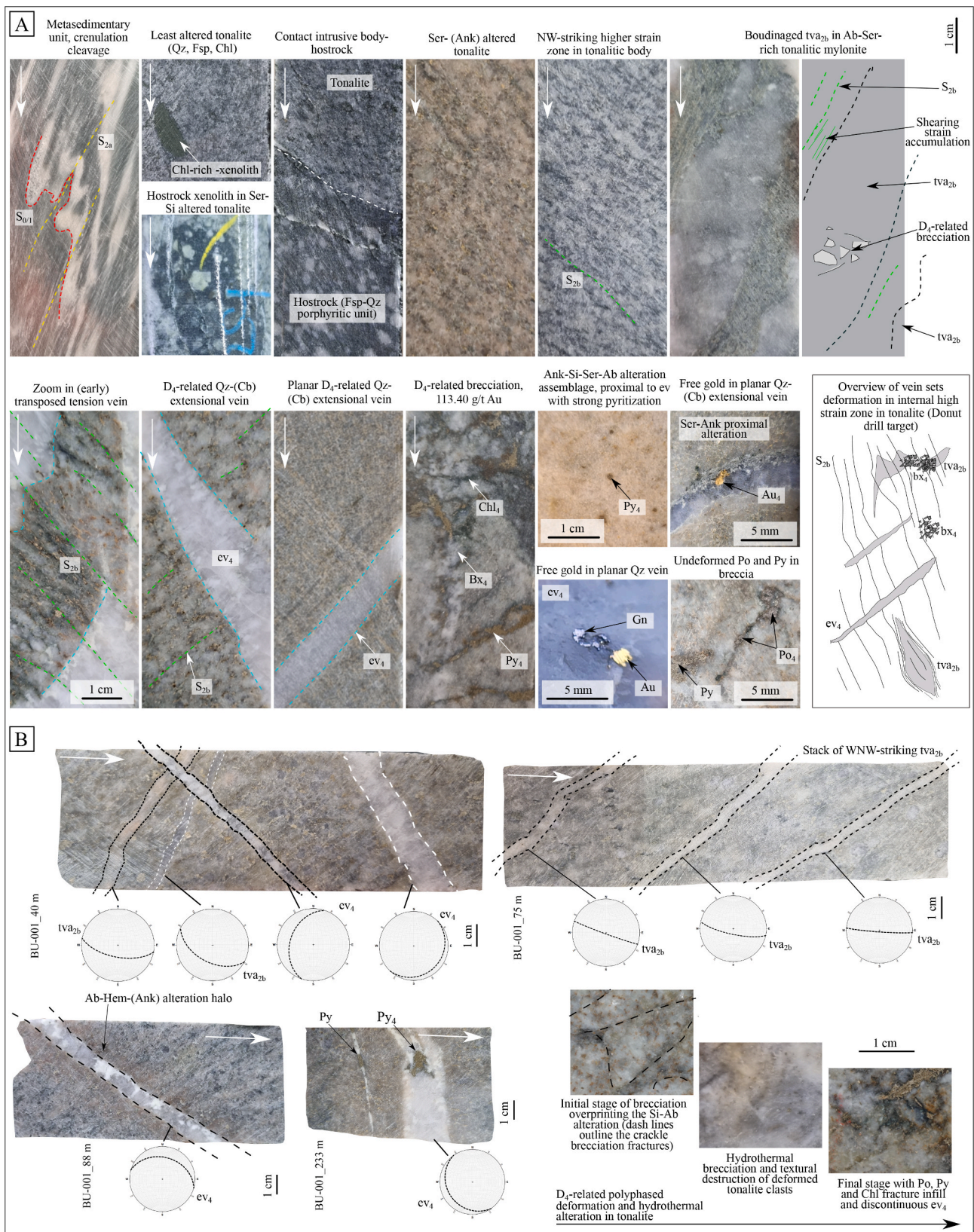


Fig. 13. A. Intrusion-hosted drill core facies from the Donut structure with emphasis on vein system and associated sulfides (A) and oriented drill cores with stereogram of mineralized veins hosted by the tonalite at the Buese deposit (B).

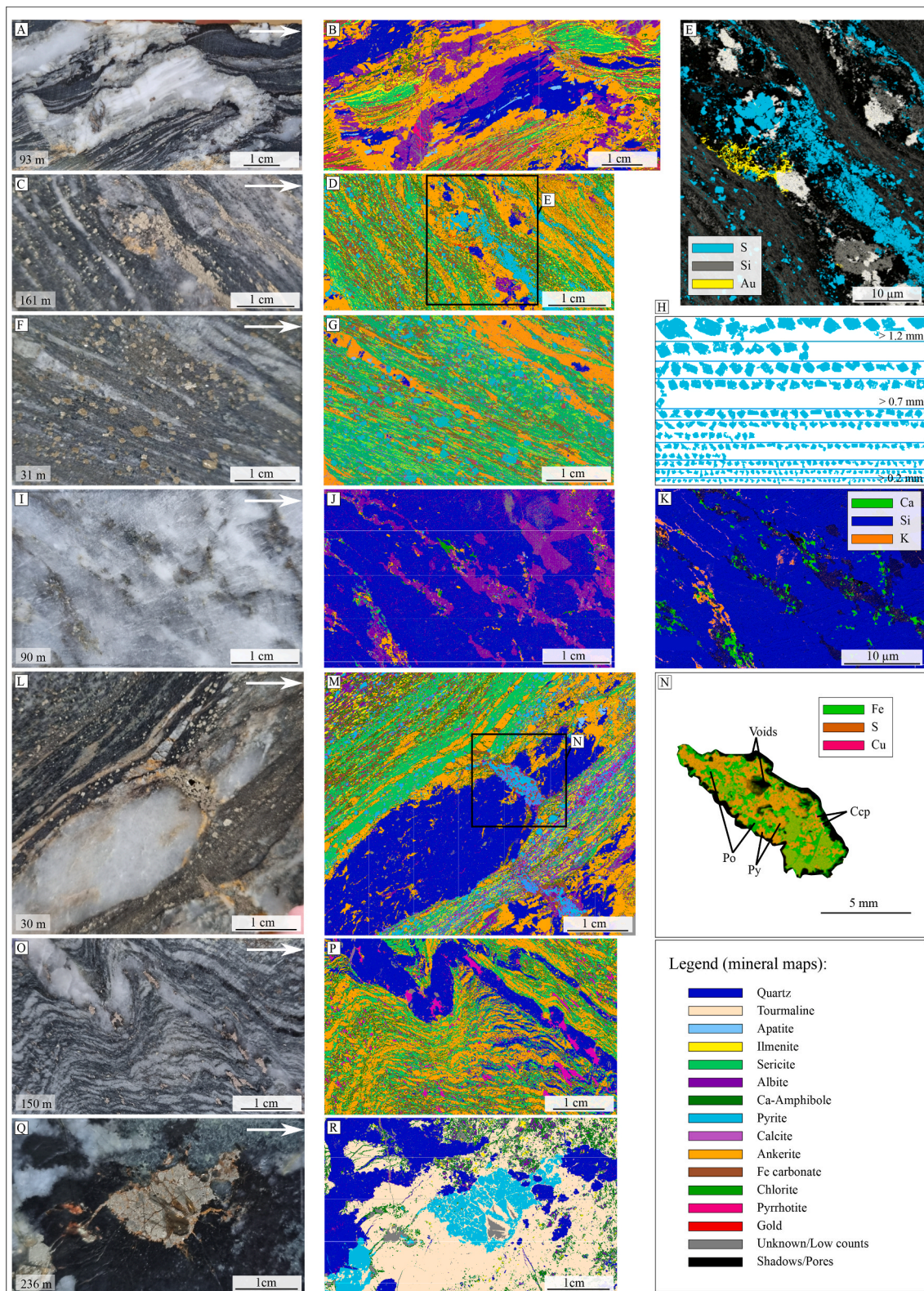


Fig. 14. Photographs (left column) and corresponding mineral map (central column) derived from μ XRF (micro-X-ray fluorescence), using Bruker AMICS mineral identification software for shear zone-hosted mineralization (Froyo structure) with A-B, the early Ab-Qz-Ank transposed vein. C-D-E, the boudinaged tva_{2b} with Py and Au deposition in dilational site (i.e., the boudin neck). F-G-H, the mylonitic facies with strong Ank-Ser alteration and rotated Py_{2b} grains (see H for grainsize distribution). I-J-K, the metric fault-fill vein with host rock slivers made of Ab-Amp-Chl-Ank. L-M-N, the boudin neck of boudinaged tva_{2b} with Po_3 - Py_3 grains. O-P, the D_3 folding of the tva_{2b} and mylonitic foliation with alternating Ank and Ser-rich layers, and Po_3 preferentially located in hinges. Q-R, the D_4 -related breccia with a Tur-Py-Chl-Qz alteration assemblage.

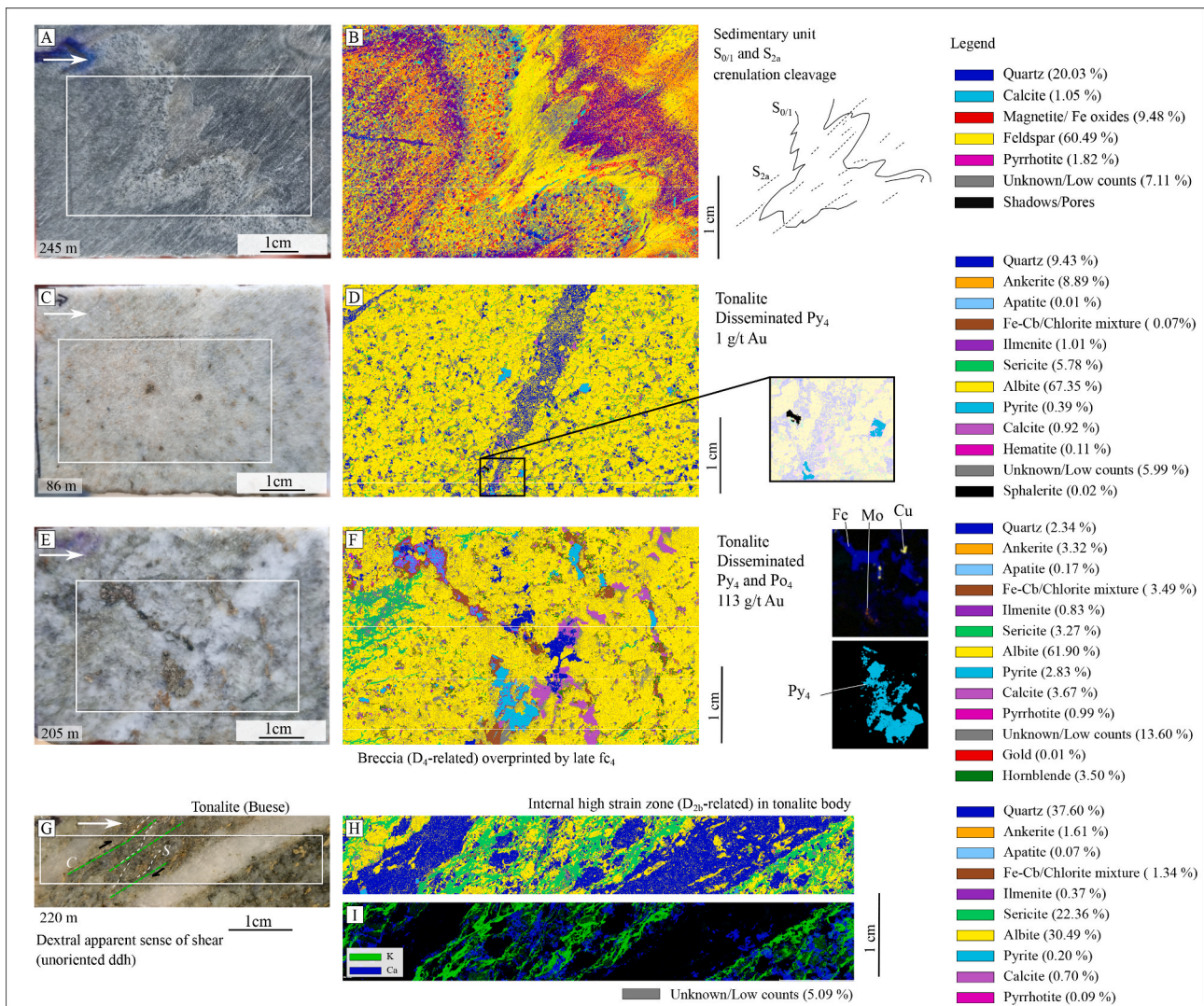


Fig. 15. Mineral map derived from μ XRF (micro-X-ray fluorescence), using Bruker AMICS mineral identification software for the intrusion –hosted mineralization (Donut and Buese structure) with A-B, Siltstone hosting the tonalite intrusion displaying a crenulation cleavage S_{2a} and early $S_{0/1}$ fabric (the unknown/low count may correspond to graphite, undetectable with the used technique). C-D, the strongly albitized tonalite with disseminated Py_4 and related ev_4 . E-F, the strongly albitized tonalite with disseminated Py_4 and Po_4 . G-H-I, the sheared tonalite (metric high-strain zone within the tonalite body) with Ser proximal to shearing and Qz-Ab veins at a low angle to the shear fabric, exhibiting some internal Ab layers subparallel to the S_{2b} fabric.

striking. The progressive folding of initially sub-horizontal tension vein arrays (tva), when incrementing the NE-SW shortening, creates folded tension veins with sub-horizontal fold axis (Fig. 6A; see the macroscopic section for details). At the deposit scale, the folding of the entire shear zone (D_{2b} -related) is also observed based on the drilling of the structure (Fig. 6A), implying a horizontal NE-SW orientation for the dZ axis of shortening and an NW-SE orientation for the intermediate incremental strain axis dY (also sub-horizontal; Fig. 6B) and continuous deformation marked by the folding of the mylonitic structure. A third folding episode (D_3 -related) is observed, where both the shear fabric and the *syn*-shearing tension veins are folded (Fig. 6C, see detailed description at the mineral scale).

Gold grades from drill core assays show that the mineralization is steeply NE dipping following the general N320 trend, with multiple mineralized intervals in the hanging wall of the main shear zone (Fig. 6D). The ore shoots are sub-horizontal and repeated at depth, as visible in Fig. 6E. Within the discrete subparallel shear zones, the mineralized intervals are located where the lithological contacts are the more frequent and with complex contact morphologies (Fig. 6F with, for example, 35 m @ 2.4 g/t Au associated with repeated porphyritic

andesite-basalt-amphibolite lithological contacts, preferential sites for enhanced deformation, hydrothermal alteration and sulfide deposition.

Oriented core measurements are summarized in Fig. 7A-B. $S_{0/1}$ trajectory is mostly NW and locally ENE, while the penetrative foliation S_{2a} and the measured lithological contacts are NW to NNW-striking and steeply dipping to NE. The folds axis of D_2 -related folding is subvertical and striking N310-330. The S_{2b} shear plane strikes N320/75–85 (sub-vertical mineral/extension lineation on shear plane, implying dip-slip shearing, NE side up) and locally reuses the preexisting fabrics. The shearing phase is identified as late to post F_{2a} folding (Fig. 3C). The local bending and deflection of the shear fabric (asymmetric folding) are poorly recorded at this scale (see drill core scale description), but the collected measurements demonstrate a N220-striking axial plane. The tension vein arrays tva_{2b} are transposed into the shear fabric and, therefore, subparallel to the S_{2b} , with sub-horizontal fold axis (5–10° dipping to the NW) for the folded tva_{2b} . Late tva_{2b} and post-shearing extensional veins are NE-striking and shallow dipping (Fig. 7B). Finally, the D_4 deformation stage is demonstrated by late fractures and single planar extensional veins are gently dipping and NNE to ENE-striking.

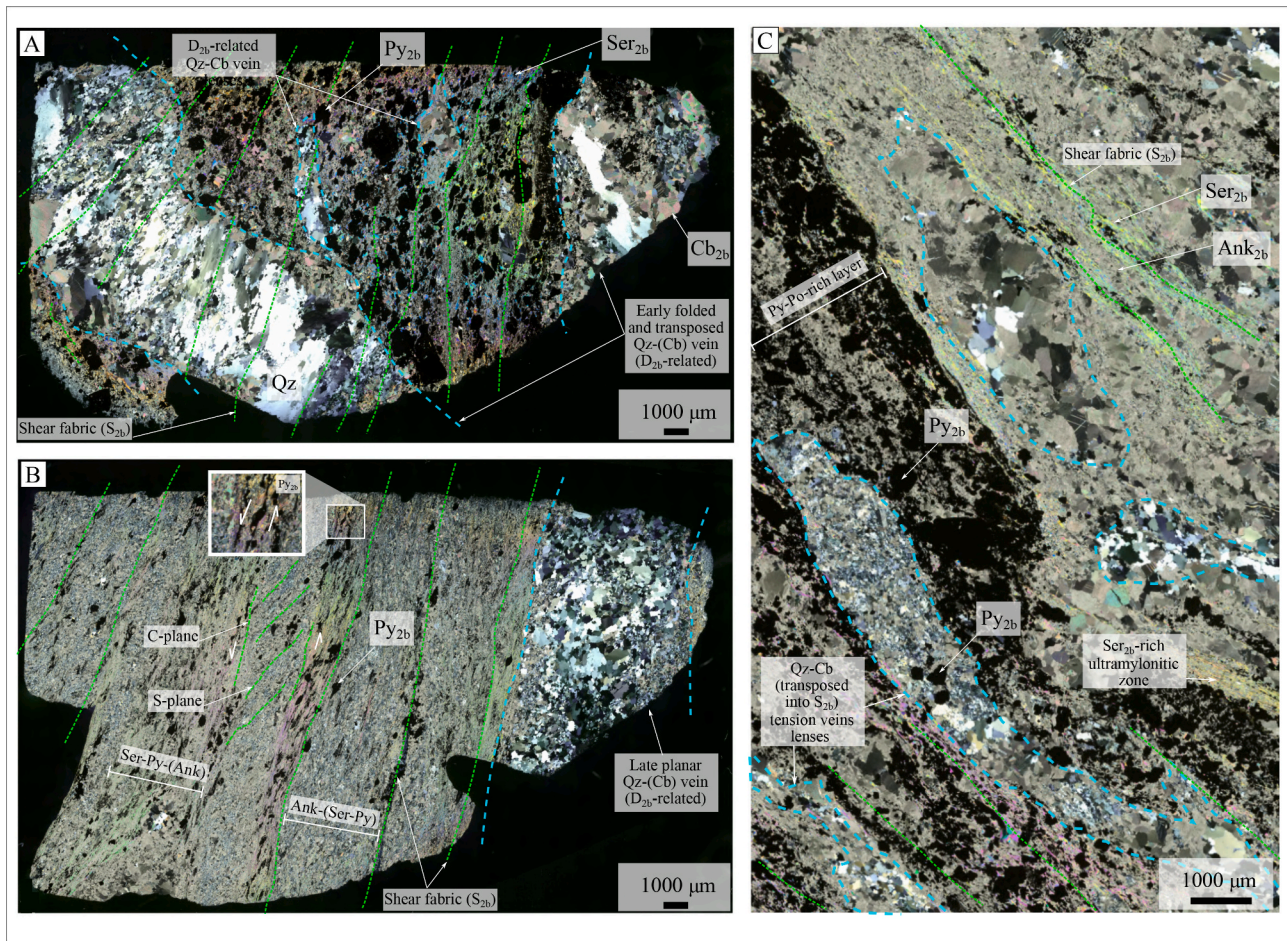


Fig. 16. Microphotographs of drill core samples (Froyo structure) under cross-polarized, transmitted light with A. Folded tension vein with S_{2b} fabric crosscutting the vein, B. Ultramylonitic facies with strong grain size reduction and Ser and Ank-rich layers, rotated and elongated Py_{2b} grains and late planar tva_{2b} reusing the shear plane, and C. Dismembered tva_{2b} with strong pyritization.

4.3.3. Geometry of the Donut target

At the Donut drill target (Fig. 4C, D), the gold mineralization is hosted by a subrounded 250 m wide tonalitic intrusive body with drill core intervals returning assays such as 19 m @ 14.23 g/t and 45 m @ 2.16 g/t Au. The shape of the intrusion varies from metric dykes to NW, following the NE limb of the Upper Antino fold, to a larger pluton in the central part of the drill target, and remains open to the NE (Fig. 4C) intruding the porphyritic andesite and the siltstone with local deflection of the $S_{0/1}$ and S_{2a} at contact. Strain is accumulated at contact (Fig. 4C-D) but also inside the intrusive body with internal discrete and metric NW-striking, SW-dipping high-strain zones (Fig. 5C) that locally bend and follow the high chargeability lineaments (Fig. 4C). No recording of the S_1 or S_{2a} foliation has been observed in the tonalite. Syn- D_{2b} shearing centimetric WNW-striking Qz-Cb tension vein arrays (locally sigmoidal-boudinaged) and planar undeformed D_4 -related extensional Qz-Cb vein (mostly NE and NW-striking, Fig. 4D) are developed in the tonalite and at the edges of the intrusive body. No oriented drill hole was available at the Donut drill target for this study.

4.3.4. The Buese deposit

The Buese gold deposit (Fig. 2A) is located on the NE limb of an antiform with NW-plunging fold axis and correlates with a camp-scale axial trace intersection (Fig. 2A). At Buese, a WNW trend of tonalitic bodies is identified (Fig. 8A) and corresponds to resistivity low domains (compared to the volcano-sedimentary host rock). The dominant penetrative foliation S_{2a} in the host rock is oriented NW-SE. Multiple high-strain zones are mapped: (1) at contacts between tonalitic plutons and

the siltstone and (2) inside the tonalite bodies, striking NW, WNW, NNW and NNE. A cross-section of the central part of the Buese deposit is given in Fig. 3B where the tonalite intrusion preferentially hosts both D_{2b} and D_4 -related extensional veins (tva_{2b} and ev_4 , respectively).

At Buese (Fig. 8C), the gold mineralization is hosted by a 300×150 m wide tonalitic intrusive body characterized by homogeneity in the Qz-Cb-Ab vein density (Fig. 8D-E-F) in the whole exposed area (mined open pit with saprolitic and locally fresh rock exposures). The host rock is composed of siltstone and minor mafic volcanic saprolite. A total of 11 metric discrete higher strain zones are identified inside the intrusive body (orientations ranging from NW to WNW to NNE that correspond to the strike of resistivity-based lineaments). A dip-slip shearing sense is observed for these internal high-strain zones with well-developed sub-vertical extension lineation on shear planes (e.g., 77/162 in the central part of the mapped intrusive body). The auriferous veins are developed adjacent to these strain accumulation zones and in between, where more brittle deformation is recorded. A total of four vein sets are mapped (Fig. 8C-D-E), with (1) NW-striking steeply dipping to the NNE, centimetric Qz-Ab-Cb, D_{2b} -related tension veins forming a stack of Py-rich, gold-bearing veins (Fig. 8D), (2) sigmoidal, NE-striking SE-dipping Qz-Ab-Cb, D_{2b} -related tension veins (Fig. 8D), (3) rare (one occurrence) mineralized metric NNE-trending Qz, D_{2b} -related fault-fill vein with host rock slivers observed in a NNE-striking high-strain zone inside the tonalite and (4) late (D_4 -related) auriferous flat centimetric Qz-Cb extensional vein dipping gently to the E. These extension veins occur as individual veins, sheeted vein arrays, and extension vein stockworks (with two main orientations locally forming a ladder vein system,

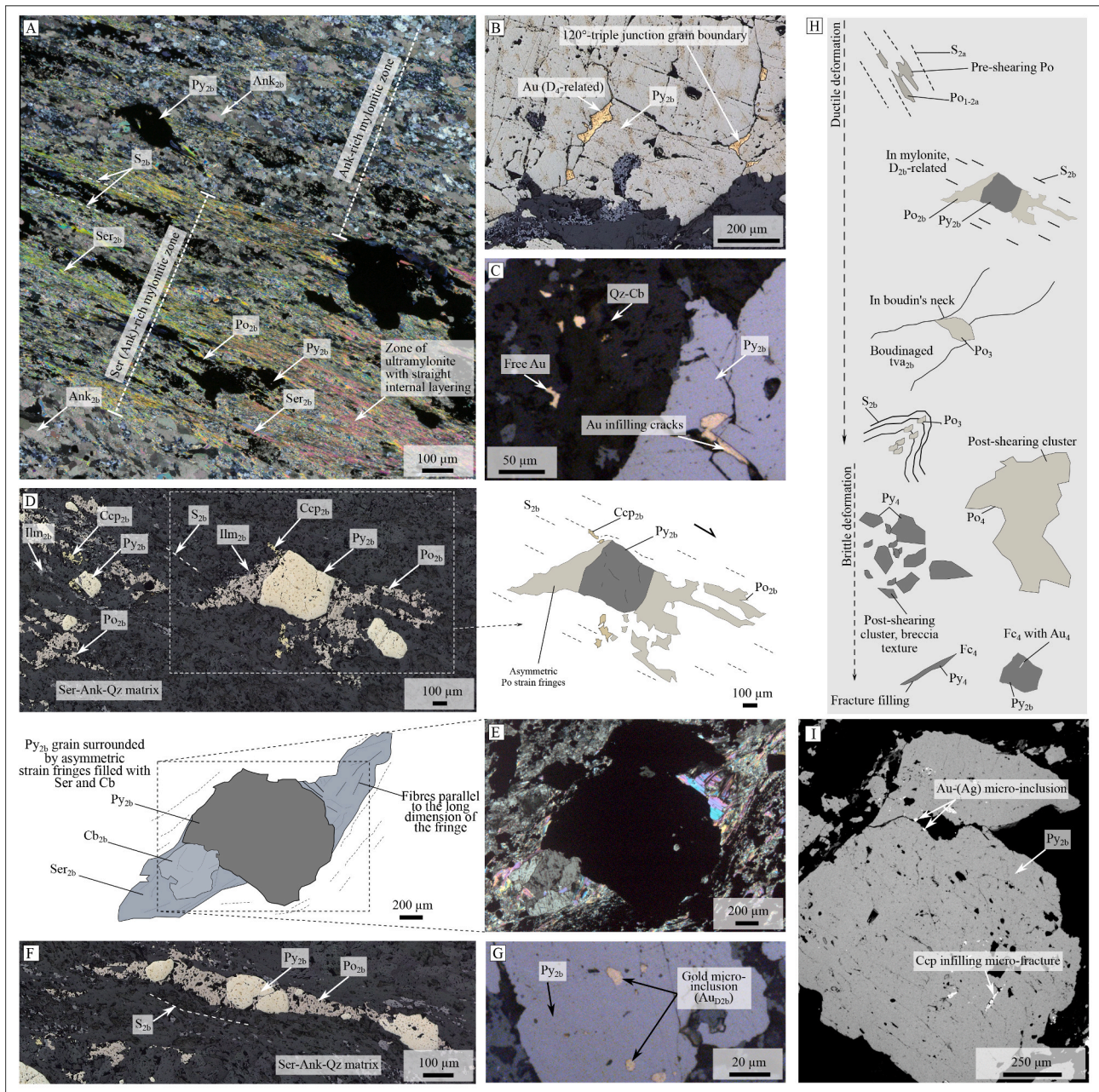


Fig. 17. Main ore features of the studied samples with microphotographs of drill core samples (Froyo structure) under cross-polarized, transmitted light (except I, SEM, BSE image). A. Disseminated Py_{2b} grains in Ser-Ank mylonite. B. Gold micro-inclusions in Py_{2b} fractures, responsible for the bulk of the mineralization. C. Free gold in Qz-Cb matrix and gold infilling cracks in Py_{2b} . D. 500 μm -wide Py_{2b} grains with asymmetric Po strain fringes in a Ser-Ank-Qz mylonitic matrix with elongated Ccp and Ilm grains. E. Asymmetric strain fringes around a pyrite grain (Py_{2b}) with Ser-Cb fibers. F. Transposed and elongated Py_{2b} grain with Po_{2b} strain fringes. G. Gold micro-inclusions in Py_{2b} . H. Overview of the textural discrimination of Py and Po and deformation history. I. Au-Ag micro-inclusions and Ccp infilling micro fractures in Py_{2b} grain. Mineral abbreviations as in Fig. 9A, (Ccp: chalcopyrite, Ilm: ilmenite).

Fig. 8F), all being interpreted as coeval except for the sub-horizontal set that appears as a later stage veining (i.e., the D_4 brittle deformation event).

4.4. Macroscopic scale expression of the deformation and associated veining, alteration and mineralization

In the Froyo drill core, mineralized zones are typically associated with a high vein density and associated sulfide deposition (example of relog of drill hole 23FRDD025 in Fig. 9A located in the central part of the map in Fig. 4A). Importantly, the D_3 -related folding of the S_{2b} shear fabric and tva_{2b} is associated with gold grades ranging from 0.4 to 10 g/t

Au. In comparison, the highest grades (5–500 g/t Au with 1 m drill core sample) are encountered when brittle deformation D_4 (polyphased with brecciation, veining, and fracturing) is overprinting ductile deformation D_2 (Fig. 9B). Po_4 centimetric clusters are associated with the highest gold grade. The log in Fig. 10 A and C highlights the strong link between gold content and (1) strain intensity (up to ultramylonitic state), (2) deflection of the shear fabric and (3) brittle deformation (associated sulfide deposition). Gold contents in these mineralized drill core intervals include 10.5 m @ 2.8 g/t Au, 5 m @ 4.2 g/t Au, and 9 m @ 8.5 g/t Au (Fig. 10C).

An overview of all deformation and associated veining sets is given in Fig. 11. At the drill core scale, the continuous progressive ductile

deformation consists of two shortening deformation stages (D_1 and D_{2a}) producing the crenulation ($S_{0/1}$ and axial plane S_{2a} , marked by Chl and Ep) with locally some transposed Po (Fig. 12). The shearing S_{2b} is accompanied by a strong sulfidation and grain size reduction; and characterized by subvertical extension lineation on shear plane marked by elongated pyrite grains. Sericitization is the main hydrothermal alteration related to the D_{2b} shearing, while ankerite is the main proximal alteration to the D_2 veining and tourmaline is observed in fault-fill vein and associated with post-shearing deformation (together with chlorite). The metric laminated fault-fill vein displays host rock slivers and tourmaline fibers parallel to the slip direction. Pronounced deformation at early vein edges is observed with strain accumulation and sulfide deposition preferentially located at one of the vein edges only, possibly forming a barrier for fluid flow. The ongoing strain during D_{2b} is indicated by the folding of the *syn*-shearing tension vein arrays initially sub-horizontal.

Discontinuous brittle deformation is expressed by millimetric fractures filled with Chl and Po . The D_4 brittle deformation is preferentially recorded in metric fault-fill veins and in localized parts of the shear zone (see discussion). Along with the fractures and centimetric NE-striking extensional veins, the D_4 deformation stage is marked by crackle breccia (monogenic, low matrix, fluid-related fracturing, host rocks being not totally disrupted) and corrosive wear/fluid replacement. Some centimetric tectonic breccia (grain reduction and oriented fragments) are also observed with two principal orientations of fractures, only one carrying Py.

In this structural framework, ore-related phases discriminated at the drill core scale by textural observations are presented in Fig. 12. The earliest Po and Py grains visible in the drill core are pre- D_{2a} and are transposed into the S_{2a} foliation. Millimetric early shearing Py_{2b} grains are sub-euhedral, rotated, locally elongated, with strain fringes, in the mylonitic zone and are spatially associated with the tv_{2b} . Elongated Po_{2b} grains are also observed in these deformed drill core intervals. Po_3 grains are identified in hinges of deflected S_{2b} (Fig. 11), and local asymmetric microfolding is a preferential site for Po deposition in hinges. Po_3 (and Py_3) are also related to (*syn*- to late-shearing) opening sites in boudin necks of boudinaged tv_{2b} (Fig. 11), where sulfide accumulation into dilational sites is created by boudinage. Clusters, stringers and fracture-infill of undeformed Py_4 and Po_4 are identified within the ductile shear zone and are clearly post-shearing. Visible free gold is commonly observed in late fractures hosted by preexisting D_{2b} -related veins and in ev_4 .

Intrusion-hosted mineralization at the Upper Antino deposit (Donut intrusion drill cores), and similarly at the Buese deposit), correlates with the strain gradient, the vein density, the brittle deformation (fracturing and D_4 -related Ank-Cb-Chl alteration) and the amount of Py and Po as illustrated in the log of Fig. 10B (relog of 24DODD007). An inverse correlation is observed between the pyrite content and the magnetic susceptibility (pyrite after magnetite, see discussion).

An overview of the main facies observed in the tonalite bodies is given in Fig. 13A, with an emphasis on the macroscopic facies of both the host lithologies (and basalt-porphyrific andesite xenoliths inside the tonalite) and the typical Ab-Ank facies of the tonalite. Quartz veins are *syn*-shearing and locally transposed into S_{2b} (shear fabric recorded in the vein) and boudinage. Brittle deformation is expressed by planar Qz-Cb vein at a high angle to the shear fabric with no recording of internal shearing and local Chl₄ and Po_4 deposition. Free gold is observed within and at the selvage of such planar veins.

Oriented cores at Buese (Fig. 13B) show that the NNE-striking vein set is late and crosscuts the stacks of WNW-striking veins. The pyritization is associated with the NW and WNW-striking veins that exhibit an Ab-Hem-Ank centimetric alteration halo. The texturally destructive brecciation is a preferential host for late vein and fracture development, indicating a polyphased deformation and hydrothermal history within the D_4 phase. The brecciation affects/offsets the early vein set while being overprinted by both the ev_4 and the late D_4 fractures. Importantly,

the tonalite's local (early D_2) silicification and albitization act as ground preparation for later deformation.

4.5. Mineral scale considerations

Detailed microstructural analysis and μ XRF drill core mineral mapping allows us to confirm and to better define the geometry at the microscopic scale.

The early- D_2 transposed veins are composed of albite and ankerite with a minor amount of quartz. Po is observed as cracks infills, oriented at 90° from the vein wall (14A and B). Due to progressive deformation of this vein set and the vein formation coeval with shearing, the veins are observed as dismembered relict (Fig. 16C), as transposed veins (Fig. 16A) with internal micro fabric and preferential orientation of grains (Fig. 14A, 18B) and as late D_{2b-c} (i.e. latest increment of ductile deformation) with planar vein, slightly transposed and re-using the shear fabric (Fig. 16B). There, the grain size is homogeneous with no recrystallization and only bulging (Fig. 18C).

High-strain zones are characterized by a strong sericitization that underlines the shear fabric with ankerite and ilmenite-rich tectonic layering (Fig. 14C and D). Ank-Qz-Ab boudins display a preferential pyritization on the lower edges of veins (Fig. 14D, E) with local redistribution of gold into boudin necks (Fig. 14E). Coarse (up to 2 mm) sub-euhedral pyrite grain (Py_{2b}) are elongated and rotated (14F, G, H) is a Ser-Ank-Ilm-rich mylonite. Banding is observed with Ank and Ser-rich domains (Fig. 16 A, B) with an important grain size reduction (millimetric Fsp phenocrysts are visible in the unshered andesitic protolith). Py_{2b} grains display asymmetrical sigma-type strain fringes (Fig. 17 A, B, C, D, H). These lower pressure regions are filled with Po (Fig. 17D, (Po after Py associated with reducing fluid conditions, high fO_2 , low pH (<6), and an increase in fluid fS_2 during the reaction) and Cb-Ser (Fig. 17 E, F). Ccp grains are found spatially associated with the Po grains (Fig. 17D) and as micro-inclusions within the rotated pyrite grains (Fig. 17I). The fault-fill veins display Amp-Chl- Po host rock slivers that are parallel to the vein wall (Fig. 14 I, J and K) with large Qz grains showing undulose extinction and irregular grain boundaries (Fig. 18A). A *syn*- (to late)-shearing redistribution of sulfides into stringers connecting boudins is observed (Fig. 14L and M) with clusters of Po_3 and Py_3 grains and Ccp inclusions (Fig. 14N), with a dilation site opening at 90° from shear slip (Fig. 14L). The margin of boudins is curvilinear and low angle to shear fabric, with fine-grained internal texture. Along this, another segregation of sulfides is identified with Po grains preferentially located in hinges (Fig. 14O) of asymmetric micro folds that postdate both the tv_{2b} emplacement and the mylonite development (bending of the Ank and Ser-rich layers in mylonitic facies) with dilation site in hinges filled with Qz. Post-shearing hydrothermal alteration is associated with Tur, Ch and Qz (Fig. 14Q, R). Gold occurs mainly as (1) free gold in Ank-Qz-Ab-Cb veins, (2) free gold within sericite-(ankerite)-rich mylonite, (3) free gold in dilation site in boudin neck, (4) micro-inclusions (D_{2b} -related) and gold infill in microfractures/cracks/grain joints within Py_{2b} grains (D_4 -related). It is worth noting that submicroscopic gold as a solid solution (lattice gold in sulfide) was not tested for this study.

At the Donut drill target, the tonalite, hosted by a crenulated siltstone (Fig. 15 A, B), shows a high albite content (about 67 % vol.) when accommodating brittle deformation (Fig. 15 C, D) with millimetric Qz veining, pyritization at vein selvages (euhedral Py grains) and less common sphalerite. Such deformation and sulfide deposition results in moderate gold mineralization with around 1 g/t grade. Locally, gold assays can be up to 113 g/t and associated with Po_4 , Chl₄, and Cc₄ (Fig. 15 E, F). In the tonalite, the ductile deformation is expressed by sericite-rich high-strain zone with related Qz-Ab tension veins (Fig. 15 E, F).

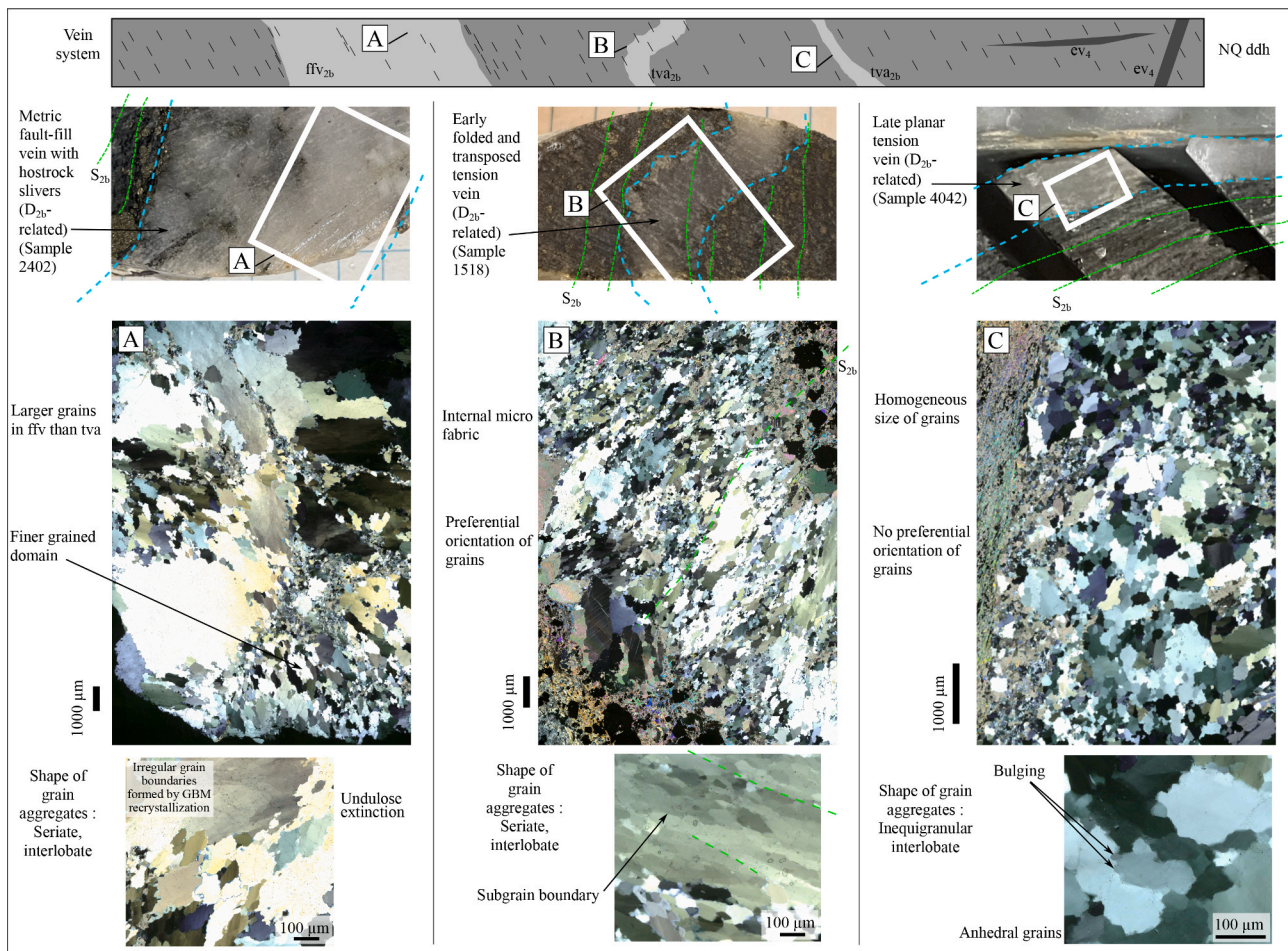


Fig. 18. Microphotographs of drill core samples (Froyo structure) under cross-polarized, transmitted light of A. The metric fault-fill vein, B. The early-shearing tension vein with internal micro fabric and preferential orientation of grains and C. The late-shearing tension vein with homogeneous size of Qz grains.

5. Discussion

5.1. The geometry of the Antino gold system, a scale-sensitive approach

This study incorporated geological and structural data collected at the district to mineral scale (Fig. 2B), with the study results highlighting that the geometry of gold systems are scale dependent. The structural framework proposed here, following the nomenclature D_x for the deformation stage creating a foliation S_x , can only be correlated at the camp to mineral scales. It is indeed impossible to correlate this deformation scheme at the craton scale and to compare it with other deposit-scale studies (Table 1) in the Guiana Shield (such as Voicu et al., 2001 for the Omai deposit in Guyana; Daoust et al., 2011 for the Rosebel deposit in Suriname; Tedeschi et al., 2018a, 2018b for the Karouni deposit in Guyana; Guiraud et al., 2020 for the Montagne d'Or deposit in French Guiana; Combes et al., 2021a, Combes et al., 2022 for the Yaou deposit in French Guiana, Combes et al., 2024 for the Brothers deposit in Suriname; Lacroix et al., 2024 for the Boulanger deposit in French Guiana or Hainque et al., 2025 for the Oko West deposit in Guyana) as local paleo stress and shortening directions are mainly controlled by local TTG-like complex emplacements, locations and shapes.

The Antino-Yaou-Benzdorp gold district, located between two TTG-like complexes, is characterized by a main NW-SE-trending deformation corridor (at the W of the district, Fig. 2A) hosting both the Antino and Benzdorp gold camps. This NW-SE trend is actually the southern end of the Maroni Splay that can be traced from the Sabajo deposit through the Brothers deposit (Combes et al., 2024) and toward the Antino-Yaou-Benzdorp gold district going south (Fig. 1B, C). At the AYW district scale,

the NW-SE compression (D_3) could be linked to the sliding and convergence of the western TTG complex towards the SE while during D_2 this same TTG seems to act as a buttress (favoring folding with NE-SW shortening, Fig. 19A). The deflection/folding of the ENE-striking primary fabric can result from the proximal craton scale CGSZ deformation corridor with its strike-slip dextral sense of shear (Fig. 1B, C; Voicu et al., 2001).

The whole district is set within the influence of this 5–10 km-wide shear structure. The ENE-striking fabrics are interpreted as the main primary foliation (the deposit scale $S_{0/1}$ of Upper Antino) resulting from the craton-scale N-S shortening (Vanderhaeghe et al., 1998; Delor et al., 2003a). The gold-bearing shear zones (second to third-order structures in the district) have their orientation parallel to the nearest TTG-like complex, witnessing (i) the strain accumulation at the margin of these TTG-like complex, and/or (ii) a ductile shearing deformation induced by the batholith emplacement (shear produced by diapiric ascent of a dome as proposed by Whitney et al., 2004 for example, but intrusion age dating is lacking in the region). The volcano-sedimentary packages are wrapped around these intrusive complexes, with the greenstone rocks recording more ductile deformation (Robert and Poulsen, 2001).

Downscaling to the camp scale, the penetrative ENE to NE-striking structures suggest an N-S- to NW-SE-oriented shortening direction. Gold occurrences at the camp scale are found at interpreted fold closures and fold limbs (Fig. 19B-C). These occurrences are hosted either within shear zones or in intrusions (Fig. 19D). The observed patterns are interpreted to result from two main deformation events, with a shift in shortening axis from NE-SW (D_{2b}) to an NW-SE orientation (D_3). Fig. 19C outlines the interpreted deformation history for the Upper

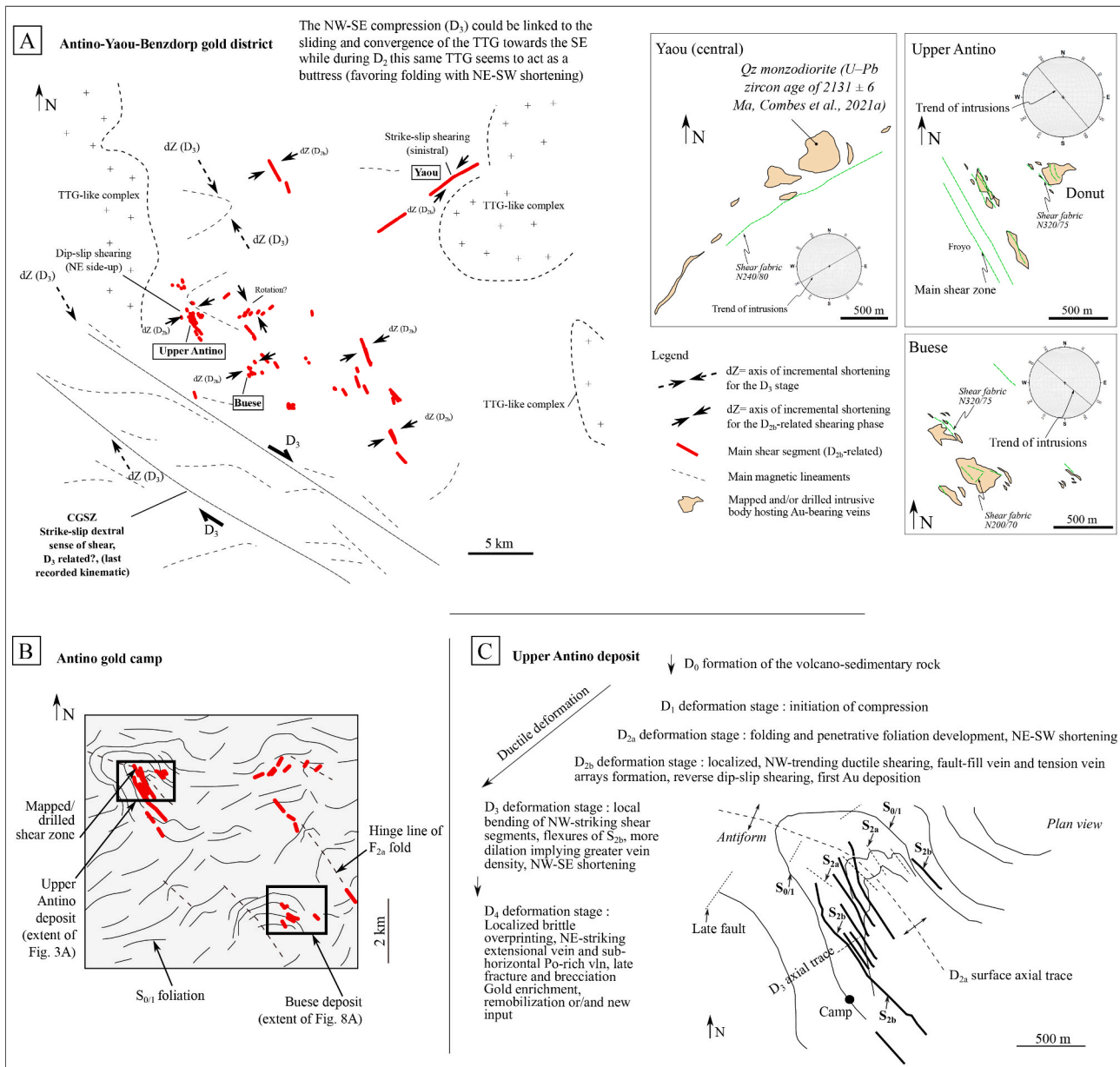


Fig. 19. Overview of main shear zones and intrusion-hosted mineralization trends within the AYB district with an emphasis on the geometry of intrusive bodies and average strike of nearest shear zone. Main interpreted shortening axis are indicated. The NW-SE compression (D_3) could be linked to the sliding and convergence of the TTT towards the SE while during D_2 this same TTT seems to act as a buttress (favoring folding with NE-SW shortening). A. Overview of the Antino gold camp where identified deposits are spatially associated with the local NW-plunging antiformal folds. B. Deformation sequence and plan view of the Upper Antino deposit. C. Sketch summarizing the structural control on gold mineralization at the deposit scale for the Upper Antino and Buese deposits. D. Flowsheet summarizing the structural control on gold mineralization at the mineral scale and expected grade for each gold event and deformation overprintings.

Antino area at the deposit scale. The ductile shear zone and the associated gold mineralization are epigenetic, as the shear segment locally crosscuts the F_{2a} fold structures. Therefore, the D_{2b} shearing cannot be only induced by a transposition in the F_{2a} fold flank. Notably, S_{2a} (axial planar to the main NW folds) and S_{2b} (mylonitic foliation) differ in their deformation styles but may be coeval or slightly sequential, with S_{2b} locally reusing the penetrative foliation. The presence of a plunging antiform, which is also observed in other areas of the district, is significant. Antiformal fold hinges, characterized by approximately 30° apical angles and overturned back limbs, are key sites for ductile–brittle deformation and gold deposition in an orogenic context (Groves et al., 2018; Goldfarb et al., 2005; Cox et al., 1995). Importantly the identified antiform at the Upper Antino deposit exhibits a NW-striking axial plane

while at the district scale the structure is localized in an ENE-striking axial plane, that could testify of a parasitic fold (Upper Antino) in a larger scale fold.

The deformation history leading to gold mineralization is as follows: The D_{2a} -related folding stage verticalized the stratigraphy while the subsequent D_{2b} -related shearing phase is preferentially recorded in the limbs. A shift in shortening axis (dZ oriented NE-SW and then NW-SE) is evidenced by the local refolding episode (D_3) reorienting the shear fabric at both metric and macroscopic scales along a NE-SW axial plane (F_3 folding). The main N320-striking shear zone at Froyo may act as a primary permeability structure, initiating the later vein and sulfide deposition. Regarding the spatial distribution of shear segments, Fig. 19D illustrates that lithological contacts serve as weak planes

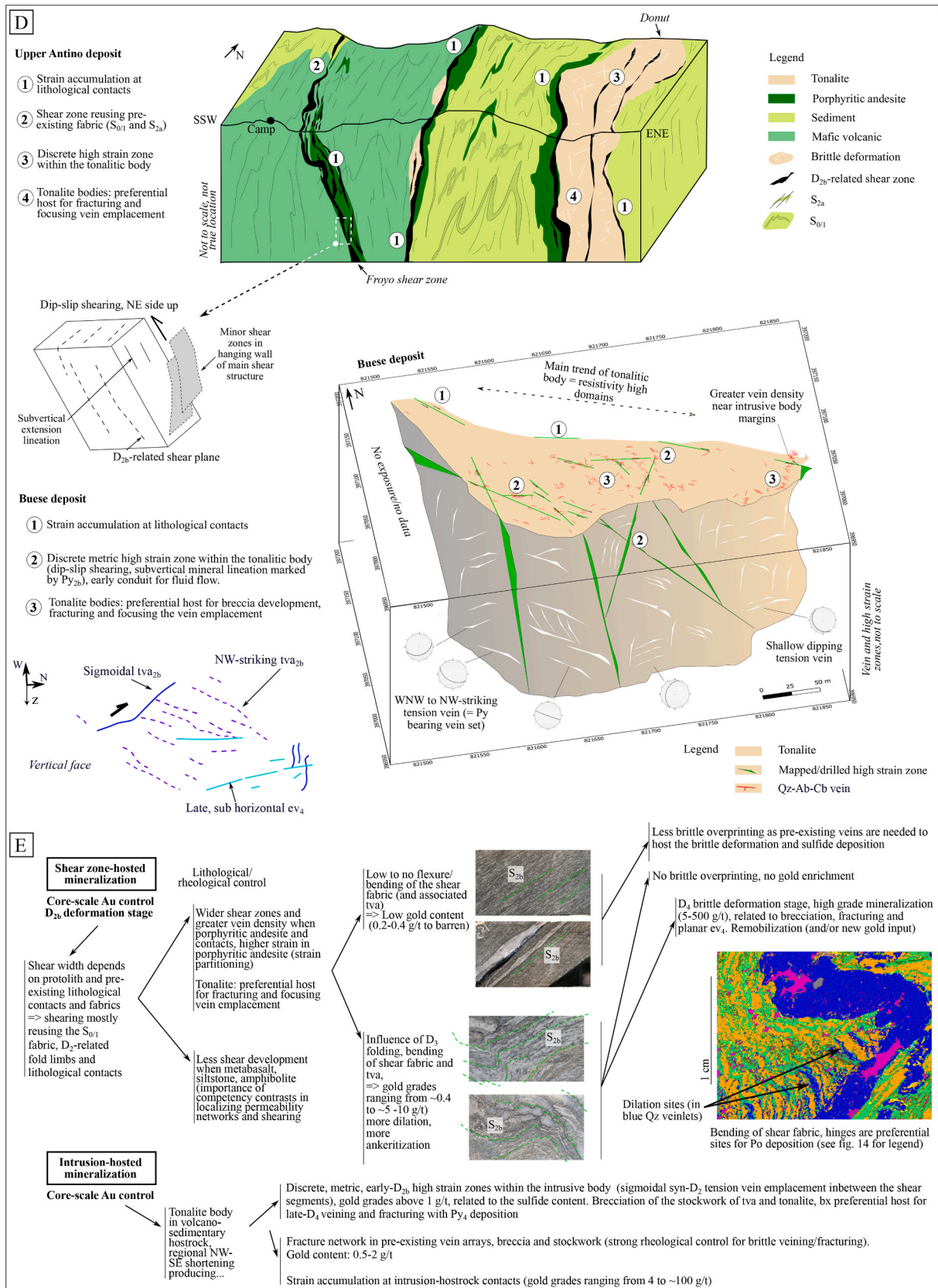


Fig. 19. (continued).

favorable for strain accumulation, fracturing and concentrating ore-bearing fluids. This progressive ductile deformation history is then locally overprinted by brittle deformation (D_4 and related vein/gold

system).

5.2. Ore shoots plunges

In reverse fault-shear systems such as the one identified at Froyo, it is important to predict the orientation and frequency of gold ore shoots. The long axis of the ore shoots is typically perpendicular to the extension lineation on the fault plane (Nelson, 2006). These ore shoots generally appear sub-horizontal and can be repeated at depth and, therefore, orthogonal to the subvertical extension lineation on shear planes. Fluid flows are then subparallel to the intermediate stress direction (σ_2 , or dY if considering the intermediate strain axis), which correlates with the permeability vector (Nelson, 2006; Cox, 2020 and references therein). However, in high-strain zones, ore shoots tend to become parallel to the slip direction, resulting in local subvertical orientations (shoot development parallel to the extension lineation marked by the elongated Py_{2b}). According to Siddorn (2011), the ore plunge can be parallel to the intersection of extensional and shear veins or orthogonal to the extension lineation, and it may align with the intersections of extensional veins and boudinaged veins. Here, the intersection of subvertical fault-fill veins with late post-shearing NE-striking extensional veins can produce additional ore shoots with subvertical plunges (plunge axis: 59/346, see stereogram Fig. 8B). Additionally, gold enrichment is also observed at the hinges of NE-striking folds related to the D_3 deformation stage (see next section) and along the boudin neck axis of boudinaged tva_{2b} , sub-horizontal axis representing (Po-Au-rich) low-stress sites.

At the mineral scale, gold is associated with (i) elongated, rotated and transposed Py_{2b} grains, (ii) Po_3 found in fold hinges of mylonite and boudin necks of early D_2 tva, and (iii) in domains that have undergone brittle deformation with D_4 -related alteration (Po_4 , Py_4 and free Au_4 in Qz-Cb matrix and in fractured Py_{2b}).

5.3. Influence of bending/deflection of shear segments on the gold concentration

The gold content on drill core intervals directly correlates with the amount of ductile deformation recorded by the mylonitic foliation and associated *syn*-shearing tva_{2b} (Fig. 10A). The *syn*- to late-shearing folding of gold-bearing mylonite was previously described by Feybesse et al. (2006) in the Ashanti Belt Ghana, (among others). At Antino, this enrichment is spatially and temporally associated with the D_3 -deformation stage (Fig. 2B, Fig. 9B, Fig. 10). The pattern of IP-based lineaments, with bending of the NW-striking high and low chargeability (and resistivity), producing NE-oriented axial traces (Fig. 4A, B), correlates with the folding of the shear fabric observed in outcrops (Fig. 5D, 6C) and in drill cores. A positive correlation is observed at the deposit scale between ore zones and the presence of D_3 -related deflection of the shear segment and, at the drill core scale, between the gold content and the observed folding of the mylonite. As presented in Fig. 19E, the gold grade can be predicted when assessing the degree of folding of the mylonitic foliation and tension veins. Drill core intervals with low to no flexure of the fabric will return grades below 0.4 g/t Au, while the influence of the folding of the shear fabric will give grades ranging from 0.4 to 10 g/t (possibly remobilization of D_{2b} -related gold), with more dilation (veining) and ankeritization observed in the drill core interval. Detailed μ XRF mapping of folded shear fabric S_{2b} and tva_{2b} indicates the increased abundance of gold-bearing Po_3 within and near the folded shear fabric hinges. This microscopic mapping also evidences the presence of dilation sites at the hinges (infilled with Qz, see μ XRF mineral map in Fig. 19E); the development of such dilational sites being a key parameter for local gold precipitation (Cox, 2020; Blenkinsop et al., 2000). The importance of refolding and its relationship with the highest gold grade and pyrrhotite deposition has been recently described in the Guiana Shield by Lacroix et al. (2024) at the Boulanger deposit in French Guiana, where the refolding is characterized by the transition from a coaxial shortening phase to a transcurent deformation event. No clear evidence at Antino was identified for such a change in deformation kinematics, but a switch in paleo stress direction is observed, associated

with the folding of the shear fabric, higher gold content and the presence of Po_3 . Similarly, Berthier et al. (2024) mention, at the Nyanzaga gold Project (Tanzania), the crucial role of folding in localizing gold mineralization and shortening orientation that favored late strike-slip deformation, leading to the development of dilational features.

5.4. Importance of rheology for brittle overprinting of preexisting features (shear zone-hosted mineralization) and of intrusive bodies (intrusions-hosted mineralization)

The detailed mapping/logging of key features of the Antino mineralization demonstrates the importance of brittle overprinting on pre-existing fabric and veins (Figs. 11, 14, 17). The preexisting veins are creating low-stress sites that will focus the deposition of succeeding veining/sulfide deposition (Siddorn, 2010, Siddorn, 2011, Chauvet, 2019 and references therein). At Antino, the redistribution of sulfides into stringers (Po_3) connecting the boudins (low-stress sites) is observed, as previously observed by Oliver et al (2020) at the Paracatu gold deposit (Minas Gerais, Brazil). Inside early-shearing tension veins (see Fig. 14A, B), Po-rich veins exploit these preexisting veins, often developed at a high angle to the early vein wall. Then, the geometry of the later vein system can be predicted by the geometry of the earlier deformed (folded/boudinaged tva_{2b}) vein system (NE and NW-striking, respectively). Siddorn (2011) previously expressed such rheological control on vein development with early Qz-Cb veins, helping to localize the deposition of secondary auriferous veins at the Giant and Con deposits (Yellowknife, Northwest Territories, Canada). Another example identified at Froyo is the flat-lying Po-bearing fractures/veinlets preferentially located in metric Qz fault-fill veins, which are favorable hosts for brittle deformation (Fig. 12) compared to the mylonitic host rock. Overall, early-shearing veins (more competent sites) constitute an important ground preparation (Peters, 1993), providing the necessary competence contrast with surrounding wall rock, concentrating the subsequent gold-bearing vein system.

The late brittle deformation and related clusters of Po_4 , are associated with post-shearing single planar extensional veins at both the Upper Antino and the intrusion-hosted Buese deposit. These veins and related sulfides are closely associated with the visible gold grains observed at Froyo (Fig. 12) and the highest gold grades, possibly caused by remobilization. Early deposition of low-grade gold mineralization followed by the development of high-grade gold during later brittle stages is commonly described in orogenic gold deposits (Simard et al., 2013; Velásquez et al., 2014; Fougereuse et al., 2016; Hastie et al., 2020; Combes et al., 2021a, 2024; Masurel et al., 2022; Thébaud et al., 2022; Sumail et al., 2024 among others).

Regarding the intrusion-hosted component, the tonalite is a preferential host for fracturing and focusing vein emplacement (Fig. 19E, see next section). Although homogeneous, the vein density is greater near the margins of the plutons (Fig. 8C, 19D). Such contact zones have an increased alteration due to contact with host rock (for example, stronger silicification observed at the Donut intrusion contact with the siltstone) and display more fracturing. Within the tonalite bodies, the domain of shearing strain tends to be early when considering the tva_{2b} development in domains of shortening strain locally between the high-strain zones. Breccia tends to develop better within Si-Ab altered domains (better competence contrast), and the amount of D_4 hydrothermal and sulfide deposition is controlled by the density of pre- D_4 ductile veining (additional competence contrast).

This presence of numerous intrusion-hosted mineralization (the main identified ones are compiled in Fig. 19A), is a key characteristic of this prolific AYB gold district. Tonalite/Qz monzodiorite metric intrusions are not as frequent in other gold districts in the region when looking at available publications (Daoust et al., 2011; Kioe-A-Sen et al., 2016; Kroonenberg et al., 2016; Combes et al., 2022, 2024) and unpublished exploration reports of main gold districts in Suriname or French Guiana.

At the deposit scale, the spatial distribution of tonalitic bodies that host mineralized tension veins shows a distinct alignment of intrusions, similar to what is observed at Buese, Benzdorp, and Yaou (Combes et al., 2021a, Combes et al., 2022). The intrusions are aligned adjacent to or parallel to the shear zones, suggesting that they are either influenced or controlled by the shear structures or have been deformed and aligned due to increased deformation. This information is crucial for predictive discovery, as identifying a shear zone or an intrusion trend can help pinpoint the location of both features. In intrusion-hosted mineralization, such as in the Donut area, margins of intrusions and local complexities, such as dykes originating from plutons, also concentrate deformation, while straight segments are less favorable targets. The shortening process (D_2 -related) results in localized high-strain zones acting as conduits for fluid flow, with strain accumulating particularly at the margins of tonalite plutons and internally (Fig. 4C and 8C). The strain partitioning is evidenced in histograms of Fig. 10 with zones of dominant shear strain (D_{2b} -related) and zone of dominant shortening strain (between the high-strain zones, forming stockworks of tva_{2b} and later sub-horizontal vein sets; Fig. 8C). Extensional veins show minimal deformation when located within the high strain zone, indicating that the shearing have acted as permeability pathways but have been inactive after the vein emplacement.

To date, twelve occurrences of tonalitic intrusions hosting gold-bearing Qz vein have been identified by the authors within the district (Fig. 2A, 19A). Along this mineralization type, the typical shear zone-hosted orogenic gold mineralization preferentially developed at lithological contacts has been observed (e.g., the Froyo shear structure). However, this type may also be spatially associated with intrusions, which could act as a stress perturbator (e.g., Oliver et al., 2001), the identified fold structures being due to intrusive bodies perturbing stress trajectories (Fig. 2A) and focusing the gold-bearing fluid flows. In this case, high magnetic domains could result from intrusive bodies outcropping and/or being buried in the volcanic sedimentary package. The local folding of the ENE-lineaments identified using the LiDAR dataset (Fig. 2A) could result from the intrusion acting as a competent body that partitioned strain. The NW-plunging antiform at Upper Antino may be controlled by a buried intrusion in the central part of the deposit (high magnetic domain), developing complex structures (S_{2b}) and local strain/stress perturbations. Alternatively, the intrusion emplacement may affect the preexisting ENE fabric ($S_{0/1}$) if the intrusive event is post- D_1 .

Within the Guiana Shield, other intrusion-hosted orogenic gold deposits have been identified. The Yaou deposit (French Guiana, in the same gold district as the Antino gold camp, Milesi et al., 2003; Combes et al., 2021a) shares similar settings with Buese and Donut (tension vein preferentially developed in metric intermediate intrusive bodies); however, the presence of internal high-strain zones and a lower Ank-Ab-Hem alteration (proximal to the mineralized vein set) at Buese and Donut are the two main discriminative settings compared to the Yaou deposit. These internal shear zones have been observed at the Brothers gold deposit (north of Antino, Fig. 1B), where metric shear zones are developed with a kilometric tonalitic batholith. Their location and geometry are controlled by internal variation within the intrusion (minor variations in composition from tonalite to diorite and changes in texture/grain size; Combes et al., 2024). This strain accumulation at lithological variations (subtle variation in composition and grain size of minerals) within an intrusion has been previously identified at the Subika deposit in Ghana (Bardoux, personal communication). Overall, the tension veins are not strictly confined within the intrusions, but there is a positive correlation. Veins found outside the intrusions are also gold-bearing, but their density is lower than within the intrusion. The absolute timing of the tonalitic intrusive event at Donut and Buese is unknown at this stage, but they recorded the D_{2b} -related shearing phase with the internal high-strain zone development and shear accumulation at intrusion edges. The intrusive event is younger than the volcanic rocks as xenoliths of porphyritic andesite and basalt are visible inside the

tonalite. Xenoliths of basalt having recorded the penetrative foliation are observed in similar intrusion at Yaou, implying that the intrusive event is younger than the local deformation stage D_{2YA} (Combes et al., 2021a, Combes et al., 2022). The Yaou intrusion yields a U-Pb zircon age of 2131 ± 6 Ma (Combes et al., 2022), while the main and economic gold event hosted by the same intrusion is dated at 2105 ± 25 Ma by Re-Os isotope analyses of gold-bearing pyrite associated with post-shearing extensional veins. While no dating was undergone during this study on the Buese and Donut intrusions, field observations imply that the tonalite is older than the inferred age of mineralization and only provides a structural and a chemical trap for gold-bearing fluids (similar to observations of Allibone et al., 2004, for the Chirano gold district in Ghana; Tourigny et al., 2018, for the Edikan mine in Ghana; or Masurel et al., 2019, for the Bonikro deposit in Ivory Coast; among others). In the Guiana Shield, two gold deposits exhibit similarities to the Buese and Donut intrusion-hosted mineralization. The Aurora gold deposit, associated with the Rory's Knoll intrusion in Guyana, shows a strong rheological control and features an alteration assemblage similar to the Ank-Ser alteration observed at Antino, with strain predominantly accommodated by the intrusion's margins. The second deposit, also in Guyana, is the Omai gold deposit (Bertoni et al., 1991; Voicu et al., 1999, 2001). It is characterized by intrusive rocks dated at ca. 2107–2081 Ma (U-Pb on zircon; Norcross et al., 2000). The so-called Omai Stock, a quartz monzodiorite, like the Yaou quartz monzodiorite, postdates the regional foliation and has been affected by a later phase of brittle deformation, responsible for the network of gold-bearing tension veins (Voicu et al., 1999, 2001). In these deposits, the role of the intrusion is purely mechanical, with characteristics typical of orogenic gold deposits. The polyphase gold system identified at Antino can be classified as an orogenic gold deposit (Goldfarb et al., 2001; Groves et al., 2020 and references therein), displaying several defining features such as a gold-only metal signature (Phillips, 2022) and low sulfide content (up to 5 % volume). It also shows a spatial relationship with structures in a ductile–brittle transitional regime and is strongly associated with syn- and post-deformation quartz-carbonate veins. Although the genetic connection between the gold mineralization and the intrusion is not yet clear, the deposit appears to be more of an intrusion-hosted orogenic gold deposit rather than an intrusion-related gold deposit (Hart and Goldfarb, 2005), as there is no observed large zonation of the mineralization or the hydrothermal alteration (Hart and Goldfarb, 2005).

6. Conclusion

This study highlights the importance of a multi-scale approach to describe and interpret the geometry of an orogenic gold system, in this case of the Antino orogenic gold system, SE Suriname. At the district scale, multiple Au-bearing shear zones are identified within the intensively deformed Antino-Yaou-Benzdorp gold district. At the camp scale, it is important to identify the local folding of ENE-striking primary foliation, as the folding influences gold mineralization patterns. At the deposit scale, the morphology of the shear zones is lithology-dependent and preferentially located in the limb of NW-plunging antiform, as seen in the Upper Antino and Buese deposits. Tonalite bodies act as preferential hosts for brittle deformation and associated brecciation/veining development. At Antino, vein types include the fault-fill veins and the tension vein arrays (coeval and D_{2b} -related), which are progressively deformed and locally crosscut by single planar extensional veins (D_4 -related). Main shortening axis for the D_{2b} shearing (NE-SW shortening) and D_3 refolding of mylonitic segments (NW-SE shortening) control the location of low-stress sites and, therefore, the location and orientation of gold ore shoots. At the mineral scale, drill core μ XRF scanning reveals that early veins act as ground preparation sites for later gold deposition, with boudin necks and folded mylonite hinges serving as low-stress zones for pyrrhotite and gold deposition. The late brittle overprinting D_4 (breccia, vein stockwork and Po-Py-rich fractures) plays an essential role in the total gold budget with remobilization and/or new gold

inputs. Both shear zone-hosted, and tonalite intrusion-hosted systems witness the importance of rheology in building an orogenic gold system.

CRedit authorship contribution statement

Vincent Combes: Writing – review & editing, Writing – original draft, Formal analysis, Conceptualization, Methodology, Investigation. **Aurélien Eglinger:** Writing – review & editing, Methodology, Validation. **Pascal Voegeli:** Project administration, Validation, Funding acquisition. **Rayez Bhoelan:** Formal analysis, Validation. **Carlos Bertoni:** Validation, Conceptualization. **Colin Padget:** Project administration, Validation, Funding acquisition. **Anne-Sylvie André-Mayer:** Methodology, Writing – review & editing.

Declaration of competing interest

The authors declare the following financial interests/personal relationships which may be considered as potential competing interests: Vincent Combes, Carlos Bertoni, Pascal Voegeli, and Colin Padget are involved with the current exploration program financed by Founders Metals Inc.

Acknowledgments

This study was funded by Founders Metals Inc. and has benefited from numerous discussions with the whole Antino exploration team (Guillaume Courtois, Cleber Pinheiro, Hamel Ibbari, Marwan Bendali, Juan Jaimes, Shiva Brand Flu, Jean-Marc Rolland, Brandon Anholt, Kaue Seoane, Nicolas Bourgeon, Sarwan Jan Jan, Katie Mackenzie, Natalie Senger, Stacey Kartopawiro, Lucas de Brito, Nikita Kepezhinskias, Mark Pohutsky, Alison Strasser, Rémi Schmitt) and Rogue Geoscience (Chris Gallagher). Discussions and guidance from Brett Davis at both the core shack and in front of saprolitic exposures are gratefully acknowledged. We would also like to thank M. Bardoux for the insightful discussions in Toronto, O. Kreuzer and R. Figueiredo e Silva for their helpful reviews of the manuscript and M. Codeco for the editorial handling. Hugo Ceinturet, Lise Salsi and Valentine Charvet are thanked for their help with the drill core μ XRF mapping at the GeoRessource Laboratory in Nancy (France).

Data availability

Data will be made available on request.

References

Aitken, A.R.A., Betts, P.G., 2009. Multi scale integrated structural and aeromagnetic analysis to guide tectonic models: an example from the eastern Musgrave Province, Central Australia. *Tectonophysics* 476, 418–435.

Allibone, A.H., McCuaig, T.C., Harris, D., Etheridge, M.A., Munroe, S., Byrne, D., Amanor, J., Gyaopong, W., 2002. Structural controls on gold mineralization at the Ashanti gold deposit, Obuasi, Ghana. *Soc. Econ. Geol. Special Publication* 9, 65–93.

Allibone, A.H., Hayden, P., Cameron, G., Duku, F., 2004. Paleoproterozoic gold deposits hosted by albite and carbonate-altered tonalite in the Chirano district, Ghana, West Africa. *Econ. Geol.* 99, 479–497. <https://doi.org/10.2113/gsecongeo.99.3.479>.

Allibone, A., Blakemore, H., Gane, J., Moore, J., Mackenzie, D., Craw, D., 2018. Contrasting structural styles of orogenic gold deposits, Reefton Goldfield, New Zealand. *Econ. Geol.* 113 (7), 1479–1497.

Allmendinger, R.W., Cardozo, N., Fisher, D., 2012. *Structural Geology Algorithms: Vectors and Tensors in Structural Geology*. Cambridge University Press.

Anand, R.R., Butt, C.R.M., 2010. A guide for mineral exploration through the regolith in the Yilgarn Craton. *Aust. J. Earth Sci.* 57, 1015–1114. <https://doi.org/10.1080/08120099.2010.522823>.

Baratoux, L., Metelka, V., Siebenaller, L., Naba, S., Naré, A., Ouyi, P., Jessell, M.W., Béziat, D., Salvi, S., Franceschi, G., 2015. Tectonic evolution of the Gaoua region: Implications for mineralization. *J. Afr. Earth Sci.* 112, 419–439.

Bardoux, M., 2017. Gold mineralization of the Guiana Shield, Guiana, and Suriname, South America: Society for Geology Applied to Mineral Deposits, 14th Biennial Meeting, Quebec City, Canada, August 20–23, 2017, Excursion Guidebook FT-03, p. 19–21.

Bardoux, M., 2019. Gold settings of the Guiana shield. In: SAXI- XI Inter-guiana Geological Conference 2019: Paramaribo, Suriname.

Bardoux, M., 2022. OCSH, IH and IR rhyacian gold deposits of the Guiana shield. In: SAXI- XII Inter-guiana Geological Conference 2022: Georgetown, Guyana.

Berthier, C., Chauvet, A., Feneyrol, J., André-Mayer, A.S., Eglinger, A., McIntyre, J., Bosc, R., 2024. Refold structures of the Archaean Nyanzaga gold Project, Sukumaland Greenstone Belt, Tanzania: Precursors to the gold-bearing fault system. *J. Struct. Geol.* 187, 105233.

Bertoni, C.H., Shaw, R.P., Singh, R., Minamoto, J., Richards, J.M., Belzile, E., 1991. Geology and gold mineralization of the Omai property, Guyana. In: Ladeira, E.A. (Ed.), *Brazil Gold 91, the Economics Geology Geochemistry and Genesis of Gold Deposits*. Balkema, Rotterdam, pp. 767–773.

Bertoni, C.H., 2019. The Nivré Gold Deposit Dorlin Project French Guiana. Abstract, SAXI- XI Inter-Guiana geological conference 2019. Paramaribo Suriname.

Bierlein, F.P., Gray, D.R., Foster, D.A., 2002. Metallogenic relationships to tectonic evolution – the Lachlan Orogen, Australia. *Earth Planet. Sci. Lett.* 202, 1.

Blenkinsop, T.G., Oberthur, T., Mapeto, O., 2000. Gold mineralization in the Mazowe area, Harare-Bindura-Shamva greenstone belt, Zimbabwe: I. Tectonic Controls on Mineralization. *Mineralium Deposita* 35, 126–137. <https://doi.org/10.1007/s001260050011>.

Blenkinsop, T., Doyle, M., Nugus, M., 2015. A unified approach to measuring structures in orientated drill core. *Geol. Soc., London, Special Publication* 421, 99–108.

Blenkinsop, T.G., Oliver, N.H.S., Dirks, P.G.H.M., Nugus, M., Tripp, G., Sanislav, I.V., 2020. Structural geology applied to the evaluation of hydrothermal gold deposits. *Rev. Econ. Geol.* 21, 1–23.

Bleys, C., 1951. Kaartblad D7. Jaarverslag van de Geologisch Mijnbouwkundige Dienst over het jaar 1950: 34–49.

Betts, P.G., Williams, H.A., Stewart, J.R., Ailleres, L., 2007. Kinematic analysis of aeromagnetic data: looking at geophysical data in a structural context. *Gondwana Res.* 11 (4), 582–583.

Butt, C.R.M., 1998. Supergene gold deposits. *AGSO J. Geol. Geophys.* 17, 89–96.

Butt, C.R.M., 2015. The development of regolith exploration geochemistry in the tropics and sub-tropics. *Ore Geol. Rev.* 73.

Cassidy, K.F., Groves, D.I., McNaughton, N.J., 1998. Late-Archean granitoid-hosted lode-gold deposits, Yilgarn craton, Western Australia: deposit characteristics, crustal architecture and implications for ore genesis. *Ore Geol. Rev.* 13, 65–102.

Chauvet, A., 2019. Structural control of ore deposits: the role of pre-existing structures on the formation of mineralised vein systems. *Minerals* 9 (3), 56. <https://doi.org/10.3390/min9030171>.

Combes, V., Eglinger, A., André-Mayer, A.-S., Teitler, Y., Heuret, A., Gibert, P., Beziat, D., 2021a. In: Polyphase gold mineralization at the Yaou deposit, French Guiana. Geological Society, London. <https://doi.org/10.1144/SP516-2020-29>.

Combes V., Teitler Y., Eglinger A., André-Mayer A.-S., Heuret A., Pochon A., Cathelineau M., Gibert P. (2021b). Diversity of supergene gold expressions and implications for gold targeting in an equatorial regolith (AMG's Couriège Exploration Prospect, French Guiana). Geological Society, London, Special Publications 516.

Combes, V., Eglinger, A., André-Mayer, A.S., Teitler, Y., Jessell, M., Zeh, A., Reisberg, L., Heuret, A., Gibert, P., 2022. Integrated geological-geophysical investigation of gold-hosting Rhyacian intrusions (Yaou, French Guiana), from deposit-to district scale. *J. S. Am. Earth Sci.* 114, 103708. <https://doi.org/10.1016/j.jsames.2021.103708>.

Combes, V., Eglinger, A., Bhoelan, R., LaPoint, D., 2024. Batholith-hosted polyphase gold mineralization at the Brothers project, eastern Suriname. *J. S. Am. Earth Sci.* 133, 104740. <https://doi.org/10.1016/j.jsames.2023.104740>.

Cook, N.J., Ciobanu, C.L., Meria, D., Silcock, D., Wade, B., 2013. Arsenopyrite–pyrite association in an orogenic gold ore: tracing mineralization history from textures and trace elements. *Econ. Geol.* 108, 1273–1283. <https://doi.org/10.2113/econgeo.108.6.1273>.

Cowan, E.J., 2020. Deposit-scale structural architecture of the Sigma-Lamaque gold deposit, Canada—insights from a newly proposed 3D method for assessing structural controls from drill hole data. *Miner. Deposita* 55, 217–240. <https://doi.org/10.1007/s00126-019-00949-6>.

Cox, S.F., Sun, S.-S., Etheridge, M.A., Wall, V.J., Potter, T.F., 1995. Structural and geochemical controls on the development of turbidite-hosted gold-quartz vein deposits, Wattle Gully Mine, Central Victoria, Australia. *Econ. Geol.* 90, 1722–1746.

Cox S (2020). The dynamics of permeability enhancement and fluid flow in overpressured, fracture-controlled hydrothermal systems. In Rowland JV, Rhys DA (editors) *Reviews in Economic Geology*, v.21. Applied Structural Geology of Ore-forming Hydrothermal Systems: Society of Economic Geologists Inc, pp. 25–82.

Daoust, C., Voicu, G., Brisson, H., Gauthier, M., 2011. Geological setting of the Paleoproterozoic Rosebel gold district, Guiana Shield, Suriname. *J. S. Am. Earth Sci.* 32, 222–245. <https://doi.org/10.1016/j.jsames.2011.07.001>.

Delor, C., Lahondère, D., Egal, E., Lafon, J.-M., Cocherie, A., Guerrot, C., Rossi, P., Truffert, C., Théveniaut, H., Phillips, D., Avelar, V.G.d., 2003b. 2-3-4 In: Transamazonian crustal growth and reworking as revealed by the 1:500000 scale geological map of French Guiana. *Géol Fr.* 5–57.

Delor, C., de Roever, E.W.F., Lafon, J.-M., Lahondère, D., Rossi, P., Cocherie, A., Guerrot, C., Potrel, A., 2003a. The Bakhuis ultrahigh-temperature granulite belt (Suriname) : II. Implications for late Transamazonian crustal stretching in a revised. *Géol Fr.* 2-3-4, 207–230.

De Roever, E.W.F., Lafon, J.-M., Delor, C., Cocherie, A., Rossi, P., Guerrot, C., Potrel, A., 2003. The Bakhuis ultrahigh-temperature granulite belt (Suriname): I. petrological and geochronological evidence for a counterclockwise P-T path at 2.07–2.05 Ga. *Geol. Fr.* 2-3-4, 175–205.

Dubé, B., Gosselin, P., 2007. Greenstone-hosted quartz carbonate vein deposits. *Mineral Deposits of Canada – A Synthesis of Major Deposit-Types, District Metallogeny, the Evolution of Geological Provinces, and Exploration Methods*, Special Publications. Goodfellow W.D., 49–73.

- Enjolvy, R., 2008. Processus d'accrétion crustale et régimes thermiques dans le bouclier des Guyanes: signatures géochimiques et thermochronologiques au transamazonien (2250-1950Ma). PhD Thesis. Université Montpellier II-Sciences et Techniques du Languedoc, pp. 305.
- Feybesse, J.L., Billa, M., Guerot, C., Duguey, E., Lescuyer, J.L., Milesi, J.P., Bouchot, V., 2006. The paleoproterozoic Ghanaian province: geodynamic model and ore controls, including regional stress modeling. *Precambrian Res* 149, 149–196.
- Fleming A., 2006. Technical report Antino Gold project Suriname, South America, Prepared for New Sleeper Gold Corporation, unpublished report.
- Fougerouse, D., Mickelthwaite, S., Tomkins, A.G., Mei, Y., Kilburn, M., Guagliardo, P., Fisher, L.A., Halfpenny, A., Gee, M., Paterson, D., Howard, D.L., 2016. Gold remobilisation and formation of high grade ore shoots driven by dissolution reprecipitation replacement and Ni substitution into auriferous arsenopyrite. *Geochem. Cosmochim. Acta* 178, 143–159.
- Franklin, J., Bertoni, C. et al. 2000. The Paul Isnard gold–copper occurrence, French Guiana: the first volcanogenic massive sulphide occurrence in the Guiana Shield? In: Sherlock, R. and Logan, M.A.V. (eds) VMS Deposits of Latin America. Geological Association of Canada, Mineral Deposits Division, Special Publication, 509–542.
- Freyssinet, P.H., Lecomte, P., Edimo, A., 1989. Dispersion of gold and base metals in the Mborguene laterite profile. *J. Geochem. Explor.* 32, 99–116. [https://doi.org/10.1016/0375-6742\(89\)90050-2](https://doi.org/10.1016/0375-6742(89)90050-2).
- Freyssinet, P.H., Butt, C.R.M., Morris, R.C. and Piantone, P. 2005. Ore-forming processes related to lateritic weathering. In: Hedenquist, J.W., Thomson, J.F.H., Goldfarb, R.J. and Richards, J.P. (eds) Economic Geology 100th Anniversary Volume. Economic Geology, 681–722.
- Gaboury, D., 2019. Parameters for the formation of orogenic gold deposits. *Appl. Earth Sci.* 1–10. <https://doi.org/10.1080/25726838.2019.1583310>.
- Gibbs, A.K., Barron, C.N., 1993. The Geology of the Guiana Shield. Oxford University Press, USA, p. 246.
- Goldfarb, R.J., Groves, D.I., Gardoll, S., 2001. Orogenic gold and geologic time: a global synthesis. *Ore Geol. Rev.* 18, 1–75.
- Goldfarb, R.J., Baker, T., Dubé, B., Groves, D.I., Hart, C.J.R. and Gosselin, P. 2005. Distribution, character, and genesis of gold deposits in metamorphic terranes. *Economic Geology*, 100th Anniversary Volume, 407–450. <https://doi.org/10.5382/AV100.14>.
- Groves, D.I., Goldfarb, R.J., Gebre-Mariam, M., Hagemann, S.G., Robert, F., 1998. Orogenic gold deposits—a proposed classification in the context of their crustal distribution and relationship to other gold deposit types. *Ore Geol. Rev.* 13, 7–27.
- Groves, D.I., Goldfarb, R.J., Knox-Robinson, C.M., Ojala, J., Gardoll, S., Yun, G., Holyland, P., 2000. Late-kinematic timing of orogenic gold deposits and its significance for computer-based exploration techniques with emphasis on the Yilgarn block, Western Australia. *Ore Geol. Rev.* 17, 1–38.
- Groves, D.I., Santosh, M., Goldfarb, R.J., Zhang, L., 2018. Structural geometry of orogenic gold deposits: implications for exploration of world-class and giant deposits. *Geosci. Front.* 9, 1163–1177.
- Groves, D.I., Santosh, M., Zhang, L., 2020. A scale-integrated exploration model for orogenic gold deposits based on a mineral system approach. *Geosci. Front.* 11 (3), 719–738.
- Guiraud, J., Tremblay, A., Jébrak, M., Ross, P.-S., Lefrançois, R., 2020. Stratigraphic setting and timing of the Montagne d'Or deposit, a unique Rhyacian Au-rich VMS deposit of the Guiana Shield, French Guiana. *Precamb. Res.* 337, 105551. <https://doi.org/10.1016/j.precambres.2019.105551>.
- Hainque, P.J., Lacroix, B., Trap, P., Bertoni, C., Eckfeldt, M., Lahondes, D., Toorn, J., Goff, E., 2024. Polyphase deformation and structural controls on Rhyacian gold mineralization at the Oko West deposit, Guyana. *J. S. Am. Earth Sci.* 153, 105327. <https://doi.org/10.1016/j.jsames.2024.105327>.
- Hart, C. and Goldfarb, R. 2005. Distinguishing intrusion related from orogenic gold systems. *Proceedings of Scientific Conference on Minerals*, New Zealand.
- Hastie, E., Kontak, D., Lafrance, B., 2020. Gold remobilization: insights from gold deposits in the Archean Swayze Greenstone Belt, Abitibi Subprovince, Canada. *Econ. Geol.* 115, 241–277. <https://doi.org/10.5382/econgeo.4709>.
- Hodgson, C.J., 1989. The structure of shear-related, vein-type gold deposits: a review. *Ore Geol. Rev.* 4, 231–273.
- Holcombe, R.J., 2016. Mapping and structural geology in mineral exploration: Where theory hits the fan: Queensland, Australia, HCOV Global, 233 p., www.holcombe.net.au/book/.
- Jébrak, M., Marcoux, E., 2008. Géologie des ressources minérales. Ministère des ressources naturelles et de la faune.
- Jessell, M., Valenta, R.K., Jung, G., Cull, J.P., Geiro, A., 1993. Structural geophysics. *Geophysics* 24, 599–602.
- Klaver, M., De Roeber, E.W.F., Nanne, J.A.M., Mason, P.R.D., Davies, G.R., 2015. Charnokites and UHT metamorphism in the Bakhuis Granulite Belt, western Suriname: evidence for two separate UHT events. *Precambrian Res.* 262, 1–19.
- Kroonenberg, S.B., de Roeber, E.W.F., Fraga, L., Reis, N., Faraco, T., Lafon, J.-M., Cordani, U., Wong, T., 2016. Paleoproterozoic evolution of the Guiana Shield in Suriname: a revised model. *Neth. J. Geosci.* 95, 491–522.
- Kioe-A-Sen, N.M., van Bergen, M.J., Wong, T.E., Kroonenberg, S.B., 2016. Gold deposits of Suriname: geological context, production, and economic significance. *Neth. J. Geosci.* 95, 429–445. <https://doi.org/10.1017/njg.2016.40>.
- Lacroix, B., Lahondes, D., Hainque, P.J., Le Goff, E., Fournier, D., Hauteville, A., Gourcerol, B., Eglinger, A., André-Mayer, A.S., 2024. Gold concentration during polyphase deformation: Insights from Boulanger Project, French Guiana. *J. S. Am. Earth Sci.* 146, 105074.
- Laing, W.P., 2004. Tension vein arrays in progressive strain: complex but predictable architecture, and major hosts of ore deposits. *J. Struct. Geol.* 26, 1303–1315. <https://doi.org/10.1016/j.jsg.2003.11.006>.
- Lebrun, E., Thébaud, N., Miller, J., Roberts, M., Evans, N., 2016. Mineralisation footprints and regional timing of the world-class Siguiro orogenic gold district (Guinea, West Africa). *Miner. Deposita* 52, 539–564.
- Ledru, P., Laserer, J.L., Manier, E., Mercier, D., 1991. Le Proterozoïque inférieur nord guyanais: révision de la lithologie, tectonique transcurrente et dynamique des bassins sédimentaires. *Bull. Societ.* 162 (4), 627–636.
- Masurel, Q., Thébaud, N., Miller, J., Ulrich, S., Hein, K.A.A., Cameron, G., Béziat, D., Bruguier, O., Davis, J.A., 2017. Sadiola Hill: a worldclass carbonate-hosted gold deposit in Mali, West Africa. *Econ Geol* 112, 23–47.
- Masurel, Q., Thébaud, N., Allibone, A., André-Mayer, A.S., Hein, K.A.A., Reisberg, L. and Miller, J. 2019. Intrusion-related affinity and orogenic gold overprint at the Paleoproterozoic Bonikro Au–(Mo) deposit (Côte d'Ivoire, West African Craton). *Mineralium Deposita*, <https://doi.org/10.1007/s00126-019-00888-2>.
- Masurel, Q., Morley, P., Thébaud, N., McFarlane, H., 2021. Gold deposits of the ~15-moz Ahafo South Camp, sefwi granite-greenstone belt, Ghana: insights into the anatomy of an orogenic gold plumbing system. *Econ. Geol.*
- Masurel, Q., Eglinger, A., Thébaud, N., Allibone, A., André-Mayer, A.S., McFarlane, H., Miller, J., Jessell, M., Aillères, L., Vanderhaeghe, O., Salvi, S., Baratoux, L., Perrouy, S., Begg, G., Fougerouse, D., Hayman, P., Wane, O., Tshibubudze, A., Parra-Avila, L., Amponsah, P.O., 2022. Paleoproterozoic gold events in the southern West African Craton: review and synopsis. *Miner. Deposita* 57 (4), 513–537. <https://doi.org/10.1007/s00126-021-01052-5>.
- McDvitt, J.A., Hagemann, S.G., Kemp, A.I.S., Thebaud, N., Fisher, C.M., Rankenburg, K., 2022. U-Pb and Sm-Nd evidence for episodic orogenic gold mineralization in the Kalgoolie gold camp, Yilgarn craton, Western Australia. *Econ. Geol.* 117 (4), 747–775. <https://doi.org/10.5382/econgeo.4892>.
- Metelka, V., Baratoux, L., Naba, S., Jessell, M.W., 2011. A geophysically constrained litho-structural analysis of the Eburnean greenstone belts and associated granitoid domains, Burkina Faso, West Africa. *Precamb. Res.* 190, 48–69.
- Micklethwaite, S., Sheldon, H.A., Baker, T., 2010. Active fault and shear processes and their implications for mineral deposit formation and discovery. *J. Struct. Geol.* 32, 151–165.
- Milesi, J.-P., Egal, E., et al., 1995. Les minéralisations du Nord de la Guyane française dans leur cadre géologique. *Chronique De La Recherche Minière* 518, 5–59.
- Milesi, J., Lerouge, C., Delor, C., Ledru, P., Billa, M., Cocherie, A., Egal, E., Fouillac, A., Lahondère, D., Lasserre, J., Marot, A., Martel-Jantin, B., Rossi, P., Tegye, M., Thévenault, H., Thiéblemont, D., Vanderhaeghe, O., 2003. Gold deposits (gold-bearing tourmalinites, gold-bearing conglomerates, and mesothermal lodes), markers of the geological evolution of French Guiana: geology, metallogeny, and stable isotope constraints. *Géol Fr* 2-3-4, 257–290.
- Nelson, E.P., 2006. Drill-hole design for dilational ore shoot targets in fault-hosted vein. *Econ. Geol.* 101, 1079–1085.
- Norcross, C., Davis, D.W., Spooner, T.C., Rust, A., 2000. U/Pb and Pb/Pb age constraints on Paleoproterozoic magmatism, deformation and gold mineralization in the Omai area Guiana Shield. *Precambrian Res.* 102, 69–86.
- Oliver, N.H.S., Ord, A., Valenta, R.K., Upton, P., 2001. Deformation, fluid flow and ore genesis in heterogeneous rocks, with examples and numerical models from the Mt Isa district, Australia. *Rev. Econ. Geol.* 14, 51–74.
- Oliver, N.H.S., Thomson, B., Freitas-Silva, F.H., Holcombe, R.J., 2020. The Low Grade Neoproterozoic, Vein-Style, Carbonaceous Phyllite-Hosted Paracatu Gold Deposit, Minas Gerais, Brazil, vol 23. *Soc. Econ. Geologists, Special Publication* 2020, 101–120.
- Perret, J., Eglinger, A., André-Mayer, A.-S., Aillères, L., Feneyrol, J., Hartshorne, C., Abanyin, E., Bosc, R., 2020. Subvertical, linear and progressive deformation related to gold mineralization at the Galat Sufar South deposit, Nubian Shield, NE Sudan. *J. Struct. Geol.* 135, 104032.
- Peters, S.G., 1993. Formation of oreshoots in mesothermal gold-quartz vein deposits: examples from Queensland, Australia. *Ore Geol. Rev.* 8, 277–301.
- Phillips, N., 2022. *Formation of Gold Deposits*. Springer Verlag, Singapore.
- Ramsay, J.G., 1962. Interference patterns produced by the superposition of folds of similar type. *J. Geol.* 70, 466–481.
- Ristorcelli, S., Spencer, R. et al. 2007. Technical report update on the Las Cristinas project, Bolivar State, Venezuela: Unpublished technical report prepared for Cystallex International Corporation by Mine Development Associates, November 7, 2007, 51–64.
- Robert, F., Brown, A.C., 1986. Archean gold-bearing quartz veins at the Sigma mine, Abitibi greenstone belt, Quebec, part I, Geologic relations and formation of the vein system. *Econ. Geol.* 81, 578–592.
- Robert, F., Poulsen, K.H., Dubé, B., 1994. Structural analysis of lode gold deposits in deformed terranes: Geological Survey of Canada, Open File Report 2850, 140 p.
- Robert, F., Poulsen, K.H., 2001. Vein formation and deformation in greenstone gold deposits. *Rev. Econ. Geol.* 14, 111–155.
- Sibson, R.H., Robert, F., Poulsen, K.H., 1988. High-angle reverse faults, fluid-pressure cycling, and mesothermal gold-quartz deposits. *Geology* 16, 551–555.
- Sibson, R.H., 1990. Conditions for fault-valve behaviour. *Geol. Soc. Lond. Spec. Publ.* 54, 15–28.
- Siddons, J.M. 2010. The role of pre-existing veining in the localization of auriferous vein systems: Examples from the Canadian Shield; Prospectors & Developers Association of Canada.
- Siddons, J.P., 2011. The Giant-Con gold deposits: a once linked Archean lode-gold system. University of Toronto. PhD Thesis.
- Simard, M., Gaboury, D., Daigneault, R., Mercier-Langevin, P., 2013. Multistage gold mineralization at the Lapa mine, Abitibi Subprovince: Insights into auriferous hydrothermal and metasomatic processes in the Cadillac-Larder Lake Fault Zone. *Miner. Deposita* 48, 883–905. <https://doi.org/10.1007/s00126-013-0466-3>.

- Sumail, N., Thebaud, Masurel, Q., Petrella, L., Roux, P., Stott, C., 2024. Polyphased gold enrichment as a key process for high-grade gold formation: insights from the 10 Moz Jundee-Bogada camp (Yilgarn Craton, Western Australia). *Miner. Deposita*.
- Théveniaut, H., Freyssinet, P.H., 2002. Timing of lateritization on the Guiana Shield: synthesis of paleomagnetic results from French Guiana and Suriname. *Palaeogeogr. Palaeoclimatol. Palaeoecol.* 178, 91–117. [https://doi.org/10.1016/S0031-0182\(01\)00404-7](https://doi.org/10.1016/S0031-0182(01)00404-7).
- Tomkins, A.G., Mavrogenes, J., 2002. Mobilization of Gold as a Polymetallic Melt during Pelite Anatexis at the Challenger Deposit, South Australia: A Metamorphosed Archean Gold Deposit. *Econ. Geol.* 97, 1249–1271. <https://doi.org/10.2113/gsecongeo.97.6.1249>.
- Thébaud, N., Sugiono, D., LaFlamme, C., Miller, J., Fisher, L., Voute, F., Tesselina, S., Sonntag, I., Fiorentini, M., 2018. Protracted and polyphased gold mineralisation in the Agnew District (Yilgarn Craton, Western Australia). *Precamb. Res.* 310, 291–304. <https://doi.org/10.1016/j.precamres.2018.02.013>.
- Thébaud, N., Eglinger, A., André-Mayer, A.S., Kolb, J., 2022. Preface to the thematic issue on mineral systems of West Africa. *Miner. Deposita* 57 (4), 509–511. <https://doi.org/10.1007/s00126-022-01100-8>.
- Tedeschi, M., Hagemann, S.G., Davis, J., 2018a. The Karouni Gold Deposit, Guyana, South America: Part I. Stratigraphic Setting and Structural Controls on Mineralization. *Econ. Geol.* 113, 1679–1704.
- Tedeschi, M., Hagemann, S.G., Roberts, M.P., Evans, N.J., 2018b. The Karouni Gold Deposit, Guyana, South America: Part II. Hydrothermal Alteration and Mineralization. *Econ. Geol.* 113, 1705–1732.
- Tourigny, G., Tranos, M.D., Masurel, Q., Kreuzer, O., Brammer, S., Ansah-Owusu, K., Yao, D., Hayford, T., 2018. Structural controls on granitoid-hosted gold mineralization and paleostress history of the Edikan gold deposits, Kumasi Basin, Southwestern Ghana. *Mineralium Deposita* 54, 1033–1052.
- Voicu, G., Bardoux, M., Jébrak, M., Crépeau, R., 1999. Structural, mineralogical, and geochemical studies of the paleoproterozoic Omai Gold Deposit, Guyana. *Econ. Geol.* 94, 1277–1304.
- Voicu, G., Bardoux, M., Stevenson, R., 2001. Lithostratigraphy, geochronology and gold metallogeny in the northern Guiana Shield, South America: a review. *Ore Geol. Rev.* 18, 211–236. [https://doi.org/10.1016/S0169-1368\(01\)00030-0](https://doi.org/10.1016/S0169-1368(01)00030-0).
- Voisey, C.R., Hunter, N.J.R., Tomkins, A.G., et al., 2024. Gold nugget formation from earthquake-induced piezoelectricity in quartz. *Nat. Geosci.* 17, 920–925.
- Vanderhaeghe, O., Ledru, P., Thiéblemont, D., Egal, E., Cocherie, A., Tegye, M., Milési, J.-P., 1998. Contrasting mechanism of crustal growth: Geodynamic evolution of the Paleoproterozoic granite–greenstone belts of French Guiana. *Precamb. Res.* 92, 165–193.
- Vearncombe, J., Zelic, M., 2015. Structural paradigms for gold: do they help us find and mine? *Appl. Earth Sci.* 124, 2–19.
- Velásquez, G., Béziat, D., Salvi, S., Siebenaller, L., Borisova, A.Y., Pokrovski, G.S., Parseval, P., 2014. Formation and deformation of pyrite and implications for gold mineralization in the El Callao district, Venezuela. *Econ. Geol.* 109, 457–486. <https://doi.org/10.2113/econgeo.109.2.457>.
- Watson, T., Lapoint, D., Stewart, K., Coleman, D., 2008. Volcanism and Sedimentation: New Insight into Arc-Related Volcanism and Sediment Deposition in a Synkinematic Paleoproterozoic Basin: Rosebel Gold Mine. University of North Carolina at Chapel Hill, Northeastern Suriname.
- Whitney, D.L., Teyssier, C., Vanderhaeghe, O., 2004. Gneiss domes and crustal flow. *Gneiss Domes Orogeny* 380, 15.
- Wyman, D.A., Cassidy, K.F., Hollings, P., 2016. Orogenic gold and the mineral systems approach: resolving fact, fiction and fantasy. *Ore Geol. Rev.* 78, 322–335.